

Vertical Structure and Driving Mechanism of PM_{2.5} and PM₁₀ Aerosols in Hefei Based on LiDAR Observations (2021–2023)

Yan Yan¹, Xueliang Deng^{1,2,*}, Rui Dai¹, Qianqian Xu¹, Qinqin Huang¹, Yang Liu¹, Chunxuan Wei¹,
Jinhua Xie¹, Yanfeng Li^{1,3}, & Yan Sun⁴

¹Hefei Meteorological Bureau, Hefei, Anhui 230061, China

²Heavy Rainfall Research Center of China, Wuhan Institute of Heavy Rain, China Meteorological Administration,
Wu Han, Hubei 430205, China

³Hefei Jichenyun Information Technology Co., Ltd., Hefei 230041, China

⁴Anhui Public Meteorological Service Center, Hefei, Anhui 230031, China

Correspondence to: Xueliang Deng (dengxueliang9989@aliyun.com)

Abstract:

Aerosol pollution remains a significant environmental concern in China. However, the vertical structure and evolution of particulate matter are poorly understood due to the lack of long-term, high-resolution observations. In Hefei, the aerosols during the study period were dominated by a mixture of fine particulate matter (PM_{2.5}) and coarse particulate matter (PM₁₀), mainly originating from urban traffic emissions, industrial activities, and regional transport, with significant contributions from secondary inorganic aerosols and occasional dust events. To address the knowledge gap in aerosol vertical distribution during different pollution episodes, this study employed an aerosol LiDAR system with 532 nm band to investigate the vertical profile characteristics of aerosols, with a focus on comparing the stratification differences of optical properties between PM_{2.5} and PM₁₀ pollution events over Hefei. The seasonal and diurnal variations of aerosol profiles were investigated on polluted and clean days. The relationship between near-surface particulate matter concentrations and aerosol vertical properties was analyzed at different heights, alongside the dynamic evolution of aerosol layers during typical pollution events. Our results demonstrated that the extinction coefficient (532 nm) of PM_{2.5}-polluted days below 0.6 km was approximately three times that of PM₁₀-polluted days. In contrast, the depolarization ratio of PM₁₀-polluted episodes remains consistently higher than

28 that of PM_{2.5}-polluted cases throughout the entire observed altitude range. The differences in extinction between
29 polluted and clean days for PM_{2.5} were most pronounced below 0.9 km and subsequently decreased as altitude
30 increased, whereas the differences in PM₁₀ remained significant below 1.2 km. For PM_{2.5}, the strongest enhancement
31 appeared between 7:00 and 14:00 (Beijing time, BJT). A subtle lifting with height was observed around midday.
32 PM₁₀-polluted days were characterized by a greater vertical extension of high aerosol extinction (up to ~1.2–1.4 km)
33 but a shorter duration of strong extinction. In contrast, PM_{2.5}-polluted days exhibited a persistent but vertically
34 confined aerosol layer. The vertical wind shear (VWS) was weaker on PM_{2.5}-polluted days compared to clean days.
35 On PM₁₀-polluted days, the VWS in the near-surface layer (1000–900 hPa) was significantly stronger than that on
36 clean days, especially during the early morning and evening periods. The PM_{2.5} pollution in Hefei was mostly
37 contributed by temperature inversion and high relative humidity, while PM₁₀ pollution was driven by long-range
38 transport of aerosol particles under the cold front system and dry conditions. These findings reveal complex
39 interactions between aerosol optical properties, boundary-layer dynamics, and synoptic conditions, providing new
40 insights into the vertical air quality processes in eastern China.

41 **Keywords:** Aerosol LiDAR, Vertical profile, Heavy pollution episodes, Vertical wind shear, Fine and coarse
42 particulate matter.

43 1. Introduction

44 Air pollution remains one of the most pressing environmental challenges globally, with fine particulate matter
45 and inhalable coarse particles posing serious risks to public health and atmospheric visibility ([Chen et al., 2023](#); [Deng
46 et al., 2023](#)). Air quality is closely related to the concentration of pollutants suspended in the atmosphere ([Wang et
47 al., 2024](#)). Solid and liquid phase pollutants, known as aerosols, not only impact air quality and visibility through
48 multiple mechanisms but also affect the climate by altering Earth's radiation budget and water cycle processes ([Chen
49 et al., 2016](#); [Miao et al., 2018](#)). In China, substantial improvements in air quality have been achieved in recent years
50 through stringent emission control policies. However, severe particle pollution events still occur frequently, especially
51 in winter haze episodes and spring dust storms across the Yangtze River Delta (YRD) region ([Han and Cao 2022](#);
52 [Wang and Wang 2021](#)). To date, most studies have focused on surface-level air quality, with particular attention to
53 individual PM_{2.5} and PM₁₀ event in eastern China and urban agglomerations from ground monitoring networks ([He
54 et al., 2021](#)). These data provide critical insights into near-surface concentrations. However, they lack information on
55 the vertical distribution and formation mechanisms of pollutants, which is essential for understanding aerosol
56 processes in the troposphere ([Mehta et al., 2021](#); [Mishra and Shibata 2012](#); [Wang et al., 2018](#)).

57 While extensive ground-based monitoring has provided insights into surface-level pollution, the understanding

58 of the vertical distribution and evolution of aerosols remains limited due to a lack of long-term and high-resolution
59 vertical observations ([He et al., 2022](#); [Ou et al., 2021](#); [Shen et al., 2022](#)). The atmospheric boundary layer (ABL)
60 plays a crucial role in regulating aerosol dynamics through physical mechanisms such as turbulence, convection, and
61 mixing ([Gao et al., 2011](#); [Garratt 1994](#); [Tombrou et al., 2007](#)). As the interface between the surface and the free
62 troposphere, the ABL governs the vertical exchange of energy, moisture, and pollutants. Numerous studies have
63 demonstrated that lower ABL heights could trap pollutants near the surface, leading to elevated PM_{2.5} levels. These
64 lower heights are often associated with thermal inversions and stagnant synoptic conditions ([Liu et al., 2020](#); [Sun et
65 al., 2024a](#)). Under such conditions, limited mixing suppresses the vertical dispersion of aerosols, allowing surface
66 emissions to accumulate rapidly, particularly in urban areas with high anthropogenic activity. In contrast, strong
67 vertical mixing and higher ABL heights enhance dispersion and dilution of pollutants, which frequently results in
68 improved surface air quality ([Jin et al., 2021](#)). Moreover, interactions between the lower ABL and the overlying free
69 troposphere, including vertical wind shear, subsidence, and entrainment processes, also significantly influence
70 aerosol layering and transboundary transport ([Deng et al., 2023](#); [Li et al., 2022](#)). These interactions are significant
71 during transition periods such as the morning boundary layer growth phase or evening collapse, which strongly affect
72 aerosol vertical distribution ([Li et al., 2018](#)). Despite these known mechanisms, detailed observations of the vertical
73 structure of aerosols and their relation to meteorological dynamics remain limited under varying pollution conditions
74 and across different seasons ([Yang et al., 2025](#)). Comprehensive long-term observations are still needed to
75 characterize how meteorology influences aerosol stratification and transformation over time.

76 Active remote sensing techniques, such as aerosol Light Detection and Ranging (LiDAR), have emerged as
77 powerful tools to fill this observational gap ([Ansmann et al., 2013](#); [Chen et al., 2024a](#)). Unlike passive satellite-based
78 instruments, LiDAR systems provide high-resolution vertical profiles of aerosol optical properties at fine temporal
79 scales and under both day and night conditions, capable of capturing sub-kilometer vertical gradients and diurnal
80 variability that are critical for understanding boundary-layer dynamics ([Wang et al., 2024](#); [Zhang et al., 2020b](#)). It
81 enables continuous monitoring of aerosol structure, boundary layer formation, and pollutant layering in response to
82 atmospheric dynamics ([Fan et al., 2024](#); [Fang et al., 2024](#); [Li et al., 2024](#)). Specifically, polarization-sensitive aerosol
83 LiDAR can simultaneously retrieve extinction coefficients and depolarization ratios, which serve as indications of
84 aerosol concentration and morphology ([Cairo et al., 2024](#); [Chen et al., 2024a](#); [Kumar et al., 2024](#)). The extinction
85 coefficient quantifies the total attenuation of light caused by scattering and absorption by particles, and it is directly
86 related to aerosol optical depth and visibility ([Chen et al., 2024b](#); [Sun et al., 2024b](#)). The depolarization ratio
87 distinguishes the spherical and non-spherical particles, providing insights into aerosol types such as secondary

88 inorganic aerosols, biomass burning smoke, and desert dust. These parameters are crucial for understanding not only
89 the optical but also the physical properties of aerosols ([Chen et al., 2024b](#); [Gebauer et al., 2024](#)). However, most
90 previous studies using such measurements have been limited to short-term campaigns or case studies of individual
91 pollution episodes ([Chen et al., 2022](#); [Zhong et al., 2018](#)). These attempts often lack the long-term temporal continuity
92 and seasonal representativeness necessary for climatological or process-level understanding, particularly in regions
93 subject to strong seasonal and meteorological variability.

94 Long-term monitoring of air pollutants is essential for the comprehensive understanding of their temporal
95 characteristics ([Fan et al., 2021](#); [Xiang et al., 2021](#)). Unlike ground-based air quality monitoring networks, vertically
96 resolved data are required to evaluate the entire process of pollution events, vertical mixing, and potential long-range
97 transport ([Wang et al., 2024](#)). Passive satellite remote sensing techniques have proven useful in bridging spatial gaps
98 in air quality data, but are limited in their ability to resolve vertical structures with high temporal accuracy due to
99 their coarse resolution and fixed overpass times ([Chen et al., 2023](#)). Chemical transport models (CTMs) have been
100 widely used to simulate the spatiotemporal behavior of aerosols and their interactions with meteorology ([Wang et al.,](#)
101 [2025](#); [Xiong et al., 2023](#)). However, their accuracy is constrained by uncertainties in emissions inventories, boundary
102 conditions, meteorological input fields, and the representation of aerosol microphysics. In addition, model
103 performance varies significantly by region and pollution type ([Zhan et al., 2024](#)). LiDAR technology provides high
104 temporal resolution and fine vertical resolution measurements of aerosol and meteorological variables, including
105 aerosol extinction, backscattering, and wind profiles ([Chen et al., 2023](#); [Chouza et al., 2015](#); [Zhang et al., 2020b](#)).
106 This capability makes LiDAR particularly suitable for investigating aerosol evolution and transport within the ABL
107 and lower troposphere. Nonetheless, long-term time series analyses based on continuous LiDAR measurements
108 remain limited in the literature.

109 To address these limitations, we conducted multi-year observations using an aerosol LiDAR system in Hefei.
110 The deployed LiDAR system provides real-time vertical profiles of aerosol extinction and depolarization ratios,
111 allowing for a detailed assessment of aerosol structure under different pollution levels. This study fills the
112 observational gap in the long-term vertical characteristics of both fine and coarse particulate pollution over this region.
113 We characterized the vertical and temporal evolution of aerosol properties and linked them with pollution episodes
114 and boundary-layer processes by integrating LiDAR data with surface PM_{2.5} and PM₁₀ concentrations,
115 meteorological observations, and reanalysis products. Therefore, the objectives of this study were (1) to analyze the
116 seasonal and diurnal variations of vertical profiles with aerosol extinction and depolarization data; (2) to compare the
117 vertical structures on polluted and clean days to clarify the differences in aerosol optical properties between these

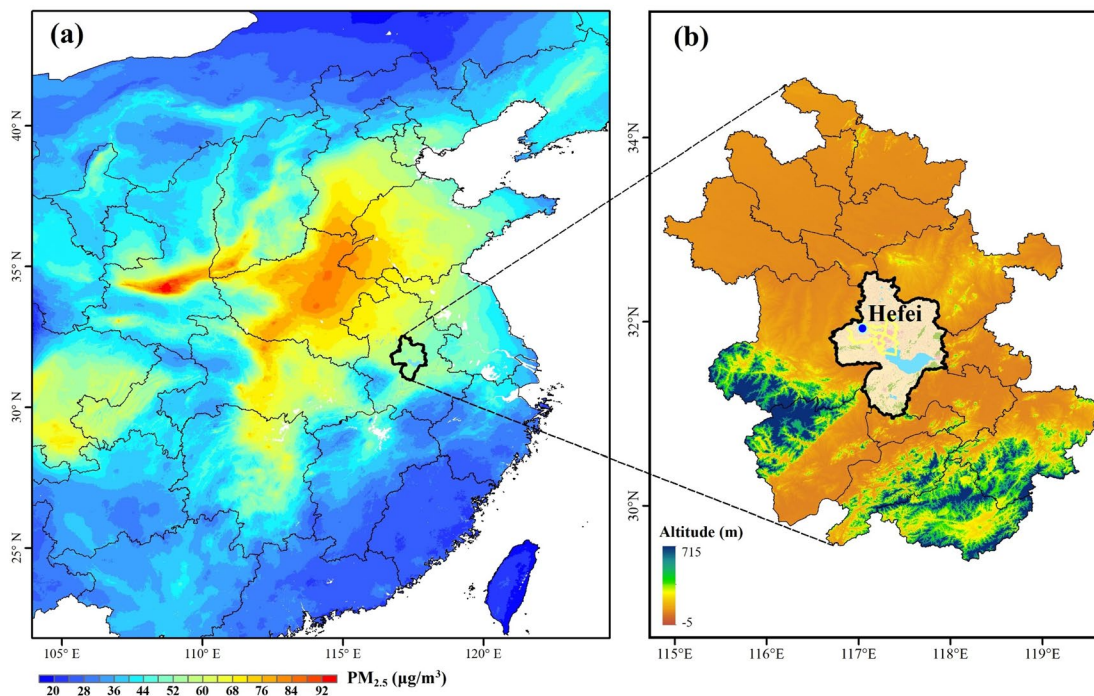
118 two conditions; (3) to assess the relationship between aerosol layering and near-surface pollutant concentrations at
119 different heights; and (4) to investigate the spatiotemporal evolution of aerosols during specific pollution episodes
120 and explore the mechanisms of their vertical structure, meteorological conditions, and accumulation process. The
121 findings are expected to enhance our understanding of aerosol vertical structure in eastern China and provide
122 scientific support for air quality management and modeling efforts.

123

124 **2. Data and methods**

125 **2.1 Study region**

126 Hefei occupies a strategic location, bridging the Beijing-Tianjin-Hebei metropolitan cluster and the Yangtze
127 River Delta economic hub. The study area lies in a transitional climatic zone, where temperature inversions occur
128 frequently in winter. Such conditions often result in stagnant air that limits pollutant dispersion. In addition, the
129 geography of Hefei plays a critical role in exacerbating air quality challenges. Hefei is surrounded by the Dabie
130 Mountains in the west and the Huangshan ranges in the south. The open plains dominate its northern and eastern
131 frontiers (**Fig. 1b**). These natural barriers hinder the southward dispersion of airborne pollutants while trapping those
132 transported from industrialized northern regions within the basin. The unique combination of geographic constraints
133 and atmospheric conditions has made Hefei a focal point for studying complex pollution mechanisms. Researchers
134 here focus particularly on the synergistic effects of regional transportation, local emissions, and meteorological
135 drivers on particulate matter formation ([Fang et al., 2024](#); [Huang et al., 2016](#); [Liu et al., 2024](#)).



136

137 **Figure 1.** The spatial distribution of (a) the averaged $PM_{2.5}$ concentration during winter from 2021 to 2023 (Ministry
 138 of Environmental Protection in China, <https://air.cnemc.cn:18007/>) and (b) the location of the study area (Hefei,
 139 China). The digital elevation model (DEM) data are derived from the NASA Shuttle Radar Topography Mission
 140 (SRTM) 30 m product (<https://glovis.usgs.gov/>), and the land use map of the study area is obtained from the 30 m
 141 resolution annual China Land Cover Dataset (CLCD) dataset. The monitoring station is marked by the blue dot.

142 2.2 Aerosol LiDAR data

143 The LGJ-05 aerosol LiDAR combines traditional radar technology and modern laser technology with 532 nm
 144 as detection light sources. Measurements at 532 nm were utilized exclusively for this study. The LiDAR emits a laser
 145 pulse into the atmosphere to capture backscattered signals, thereby obtaining key aerosol optical characteristics. As
 146 a polarization-sensitive system, it can retrieve extinction coefficients and depolarization ratios to characterize
 147 aerosols in the atmosphere. During the transmission process, the laser pulse is scattered and extinguished by
 148 atmospheric aerosol particles. The intensity of backscattered light at different altitudes correlates with the scattering
 149 and extinction properties of aerosol and cloud particles at those altitudes. The backscattered light from spherical
 150 particles can maintain its polarization characteristics of the emitted pulse since the emitted laser pulse is linearly
 151 polarized. In contrast, non-spherical particles (such as dust particles and ice crystals in cirrus clouds) depolarize the
 152 backscattered light due to their irregular shapes and asymmetric interaction with linearly polarized laser pulses. The
 153 LiDAR could detect the echo signals of the parallel and vertical components in the backscattered light, enabling
 154 acquisition of the vertical profile of the depolarization ratio of atmospheric aerosol particles. It could enable three-

155 dimensional monitoring of the atmosphere in real time through active remote sensing, with the capacity to invert
156 spatiotemporal distribution information such as aerosol extinction, depolarization, and water vapor mixing ratio in
157 the atmosphere. The aerosol extinction coefficient reflects the attenuation capacity of aerosol particles to incident
158 light, while the depolarization ratio indicates the non-spherical nature of aerosol and cloud particles. A higher
159 extinction coefficient typically indicates a larger concentration of aerosol particles or stronger light-
160 scattering/absorbing properties. However, greater depolarization values denote a higher abundance of non-spherical
161 aerosol particles (e.g., dust, rugged industrial aerosols) or mixed-phase cloud constituents. By contrast, lower
162 depolarization ratios indicate a dominance of spherical particles or simpler particle structures.

163 Since the instrument is capable of receiving data below 30 km, the effective detection range of the aerosol
164 LiDAR can cover 0.2-6 km and 0.2-15 km for daytime and nighttime, respectively. It offers a vertical spatial
165 resolution of 7.5 meters and a temporal resolution of 10 minutes. The observations were conducted at the National
166 Meteorological Observation Station in the northwest of Hefei (117.06°N, 31.96°E) from March 2021 to May 2023.

167

168 **2.3 Ground-based observational data**

169 Hourly concentrations of PM_{2.5} and PM₁₀ were obtained from ground-based monitoring stations in Hefei, which
170 are operated and maintained by the China National Environmental Monitoring Centre (CNEMC) ([Liu et al., 2017](#)).
171 These pollutant data were obtained from professional monitoring instruments, with the LGH-01E aerosol mass
172 concentration monitor used for PM₁₀ and the LGH-01B for PM_{2.5}, both of which apply the beta attenuation method.
173 All instruments are calibrated regularly according to national standards, and the data undergo strict quality control
174 procedures, including hourly, daily, and annual audits, as described in the China Environmental Monitoring Quality
175 Assurance and Quality Control Manual. It should be noted that we focused on PM_{2.5} and PM₁₀ concentrations during
176 winter and spring, respectively. All comparisons between PM_{2.5} and PM₁₀ pollution episodes were conducted across
177 both seasons. The hourly resolution of the dataset allows for capturing diurnal variations in pollutant levels, while
178 the multi-pollutant data facilitates analysis of the differences in meteorological responses of pollutants in Hefei.

179 The observed meteorological variables were obtained from the China Meteorological Administration (CMA)
180 (<http://data.cma.cn/en>), measured by the Vaisala PTB210 Digital Barometer for atmospheric pressure, the Vaisala
181 HMP155A Temperature and Relative Humidity Probe for air temperature (T) and relative humidity (RH), the EL15-
182 2C Wind Direction Sensor for wind direction (WD), and the EL15-1C Wind Speed Sensor for wind speed (WS). All
183 meteorological instruments are routinely maintained and calibrated to ensure the accuracy and reliability of
184 observational data.

185 2.4 ECMWF reanalysis data

186 This study aims to investigate the impact of the synoptic system on PM_{2.5} and PM₁₀ pollution. The ERA5
187 reanalysis dataset, freely accessible via the Copernicus Climate Change Services platform
188 (<https://cds.climate.copernicus.eu/datasets>), serves as the data source. Vertical atmospheric data within the ERA5
189 dataset are interpolated to 37 pressure levels. This interpolation yields comprehensive data ranging from the Earth's
190 surface to the upper atmosphere. Given its high spatial and temporal resolution, the ERA5 dataset has been widely
191 employed in extreme weather events, climate prediction, and air pollution studies ([Fan et al., 2021](#); [Zhang et al.,](#)
192 [2020b](#)).

193 This study collected hourly geopotential height, vertical wind velocity, temperature, and humidity data. The data
194 correspond to multi-pressure levels (500 hPa, 700 hPa, 725 hPa, 750 hPa, 775 hPa, 800 hPa, 825 hPa, 850 hPa, 875
195 hPa, 900 hPa, 925 hPa, 950 hPa, 975 hPa, and 1000 hPa). The spatial resolution of our dataset was 0.25°×0.25°
196 (zonal and meridional) and supports a detailed and accurate exploration of the synoptic-particulate matter relationship.
197 The data were extracted for winter and spring during 2021–2023, consistent with the periods of the surface pollutant
198 and aerosol LiDAR observations.

200 2.5 Quality control

201 To explore the potential of aerosol LiDAR observations and improve data reliability, this study extracted the
202 extinction coefficient and depolarization ratio data at 532 nm from the LiDAR system for the period from March
203 2021 to May 2023. In the quality control process, specific criteria were established to ensure the reliability of the
204 retrieved parameters. Specifically, it covers three steps for outlier detection, removal of spurious points, and temporal
205 consistency analysis. Outlier detection was conducted to eliminate all records outside the normal value range
206 according to the parameter intervals provided by the instrument, with specific thresholds applied based on the signal-
207 to-noise ratios (SNR) of the parallel (P) and perpendicular (S) channels. The extinction coefficient at 532 nm was
208 calculated using data from the P channel, which was considered reliable only when the corresponding SNR exceeded
209 three. The depolarization ratio was derived from the P and S channels, and data were accepted only when both
210 channels had SNRs greater than three. The P channel detects linearly polarized light in the parallel direction, while
211 the S channel detects linearly polarized light in the perpendicular direction. Based on the time series of SNR records,
212 the individual extinction and depolarization data were cross-referenced. Temporal consistency analysis was
213 conducted by identifying records that deviated by more than three standard deviations from the mean as outliers. The
214 original LiDAR data have a 10-minute temporal resolution. After quality control, these data were averaged to hourly

215 resolution to be consistent with the hourly ground-based pollutant observations. To further improve data reliability,
 216 this study calculated the credibility ratio of the extinction coefficient and depolarization ratio at different altitudes.
 217 Based on the criterion of a 60% valid data availability rate, the effective detection ranges for the 532 nm of the
 218 extinction coefficient and depolarization ratio were 0.2~1.8 km.

220 2.6 Methodology

221 2.6.1 Definition of polluted and clean

222 In this study, the data from 2021-2023 are gathered and categorized into four seasons: spring (Mar.-May),
 223 summer (Jun.-Aug.), autumn (Sep.-Nov.), and winter (Dec.-Feb.). Given that PM_{2.5} pollution is most severe in winter
 224 and sand-dust events are frequent in spring, the definitions of polluted and clean days in this study primarily focus
 225 on these two seasons. Days in winter when the daily average concentration of PM_{2.5} exceeds 75 µg/m³ are defined as
 226 PM_{2.5}-polluted days. Conversely, days in winter with a daily average PM_{2.5} concentration below 50 µg/m³ are
 227 classified as PM_{2.5}-clean days. For PM₁₀, spring days with daily average concentrations above 150 µg/m³ are defined
 228 as polluted days, while those below 100 µg/m³ are considered clean days (Ministry of Environmental Protection of
 229 the People's Republic of China, Technical Regulation on Ambient Air Quality Index, 2012). To eliminate the wet
 230 deposition effect of precipitation, all observations in this study excluded precipitation daily data.

231 2.6.2 Calculation of Vertical Wind Shear

232 The vertical wind shear (VWS) is a crucial factor in characterizing the change in wind velocity with height. It
 233 is defined as the variation of wind vector across atmospheric layers, quantified by the magnitude of the difference
 234 between upper and lower levels. The VWS can be calculated using the following formula:

$$235 \text{ VWS} = \frac{\sqrt{(u_t - u_l)^2 + (v_t - v_l)^2}}{(z_t - z_l)} \times 1000 \quad (1)$$

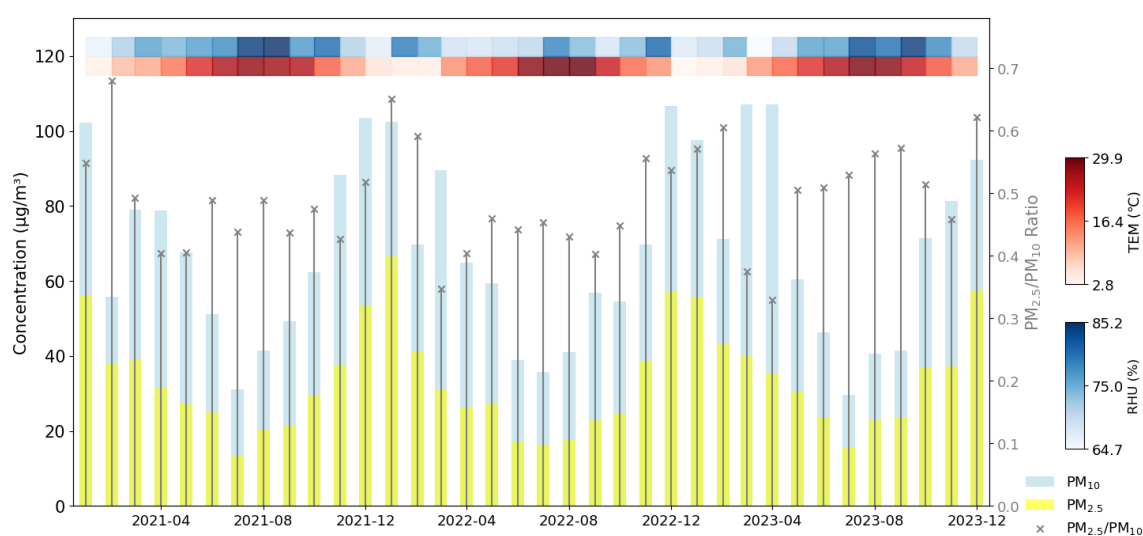
236 Where VWS is measured in units of m/s·km⁻¹. u_t and u_l denote the zonal wind components at the upper z_t and lower
 237 z_l levels, respectively, while v_t and v_l represent the corresponding meridional wind components. This calculation aids
 238 in quantifying the vertical dynamic forces that may impact the dispersion and transportation of pollutants.

239 3. Results and discussion

240 3.1 Variations of inter-annual PM_{2.5} and PM₁₀

241 **Figure 2** shows the variations in the concentrations of PM_{2.5} and PM₁₀ pollutants from 2021 to 2023. Both PM_{2.5}
 242 and PM₁₀ pollutants exhibited a clear seasonal pattern, with concentrations higher in winter and lower in summer

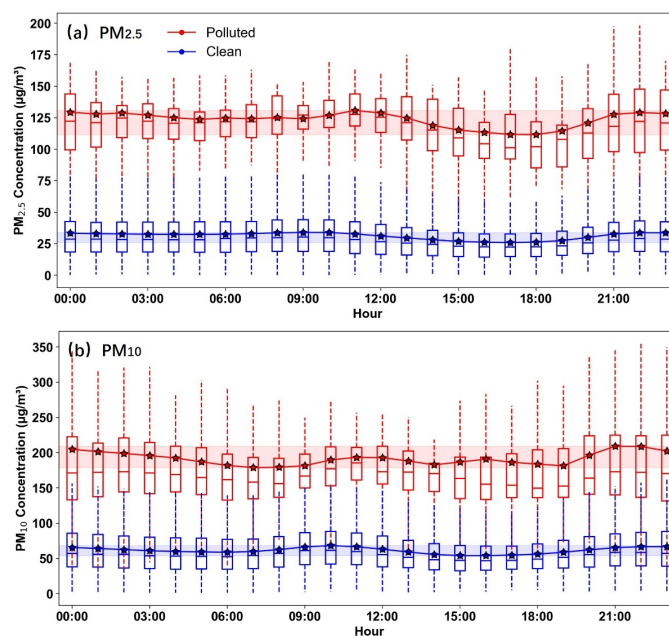
243 (Liu et al., 2021; Wang et al., 2024). In addition, PM₁₀ concentrations were relatively high during the spring months
 244 of 2022 and 2023, likely driven by increased dust events such as sand-dust storms that commonly occurred during
 245 this season. High PM_{2.5}/PM₁₀ ratios (≥ 0.5) during winter suggest a dominant contribution from fine particulate
 246 matter, whereas lower ratios (≤ 0.5) in spring indicate an increased presence of coarse particles (Liu et al., 2015).
 247 The episodic PM₁₀ peaks observed in spring 2022–2023 coincided with a pronounced decrease in the PM_{2.5}/PM₁₀
 248 ratio in Hefei. This phenomenon reflected intensified pollution of coarse-mode aerosols. Although winter months
 249 also suffered elevated PM₁₀ pollution, the concurrent high PM_{2.5} concentrations complicated the separation of dust-
 250 related contributions. In contrast, the lower PM_{2.5}/PM₁₀ ratios in spring facilitated the distinct observation of dust
 251 events due to the reduced interference from fine particulate matter.



252
 253 **Figure 2.** Monthly variation of PM_{2.5} (marked as the yellow bars) and PM₁₀ (marked as the blue bars)
 254 concentrations, PM_{2.5}/PM₁₀ ratio (the grey lines with markers on top), temperature (TEM), and relative humidity
 255 (RH) during 2021-2023 in Hefei (Beijing time, BJT = UTC + 8 h).

256
 257 The hourly PM_{2.5} and PM₁₀ concentrations exhibited clear diurnal variation on both polluted and clean days (**Fig.**
 258 **3**). Polluted days showed significantly higher PM_{2.5} levels, with hourly averages ranging from 100 to 125 µg/m³,
 259 compared to the stable 35–55 µg/m³ range observed on clean days. The PM_{2.5} concentrations on polluted days
 260 displayed a bimodal pattern. The concentrations remained consistently high throughout the morning period from
 261 04:00 to 11:00 (Beijing time, BJT), with the peak at 10:00–11:00 (BJT) (Dai et al., 2020). Valleys in PM_{2.5}
 262 concentrations occurred at 16:00 (BJT), possibly associated with enhanced atmospheric dispersion from midday
 263 heating that facilitates the dilution of particulate matter. Concentrations initiated an upward trend from 17:00 (BJT),
 264 with a gradual increase culminating in a peak between 21:00 and 22:00 (BJT). In contrast, clean days exhibited a

265 subtle morning and overnight peaks. For PM_{10} , polluted days presented pronounced peaks at 10:00–12:00 and 21:00–
 266 22:00 (BJT), coinciding with increased dust resuspension or construction activities (Yu et al., 2020). However, valleys
 267 occurred at 07:00 and 19:00 (BJT). These may be due to reduced surface disturbances during dawn and enhanced
 268 vertical mixing in the afternoon. Clean days maintained relatively low hourly mean PM_{10} concentrations (50–70
 269 $\mu\text{g}/\text{m}^3$) with minor fluctuations. The time series curves of pollutants had different peak times and amplitudes,
 270 indicating distinct origins. $PM_{2.5}$ was more influenced by continuous anthropogenic emissions, while PM_{10} was
 271 sensitive to episodic coarse-particle events (Deng et al., 2023; Wang et al., 2024). These hourly dynamics highlighted
 272 the role of diurnal meteorological cycles in modulating particulate matter distribution, with polluted days amplifying
 273 both primary emissions and secondary aerosol formation (Liu et al., 2021).



274
 275 **Figure 3.** Hourly mean (a) $PM_{2.5}$ and (b) PM_{10} concentrations on polluted and clean days (Beijing time, BJT = UTC
 276 + 8 h). The blue and red shaded areas represent the ranges of mean concentration values for polluted and clean days,
 277 respectively. The whiskers and boxes represent the 95th, 75th, 50th, 25th, and 5th percentiles, respectively. The stars
 278 represent the mean values of the pollutant concentrations. The solid lines connect the hourly mean values to show
 279 the diurnal variation trends.

280

281 3.2 Temporal variation of vertical distribution structure

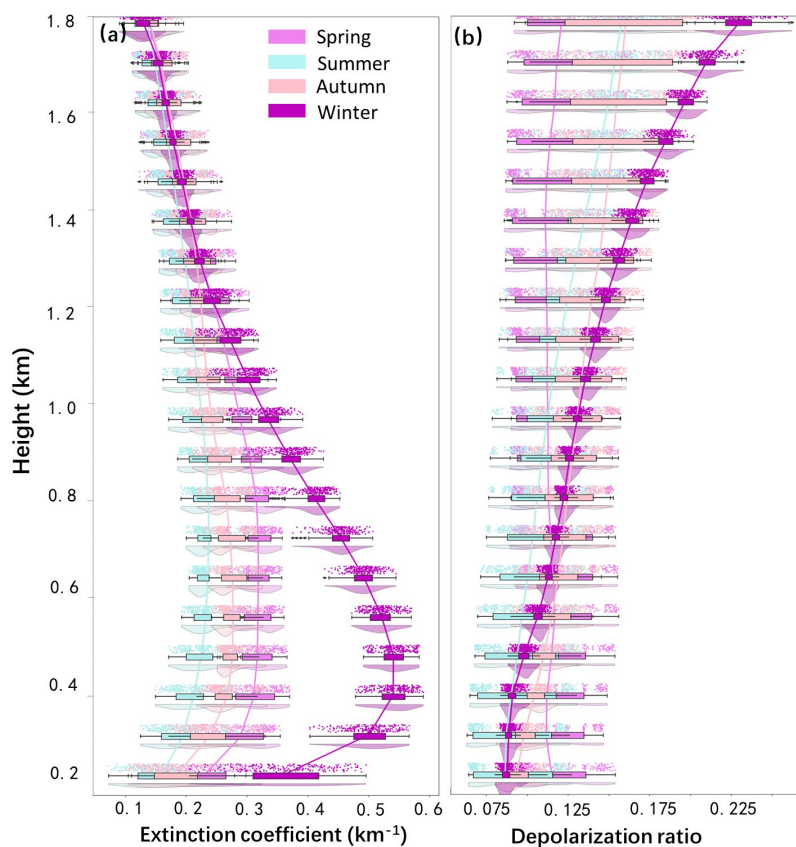
282 In addition to the impacts exerted by surface-level pollution, the investigation of vertical distribution is also of
 283 paramount significance for a comprehensive understanding of air quality dynamics. The extinction coefficient at 532
 284 nm shows seasonal and vertical variation. Vertically, extinction coefficients were highest near the surface and

285 gradually decreased with altitude in all seasons. This vertical decline arises from rapid reductions in aerosol loading
286 due to vertical mixing, gravitational sedimentation, and dilution with increasing height, as well as the dominance of
287 weaker molecular scattering above the planetary boundary layer ([Wang et al., 2021](#)). Winter presented the highest
288 extinction values among the four seasons (**Fig. 4a**) ([Chen et al., 2023](#); [Wang et al., 2024](#)). This was likely related to
289 enhanced emissions from domestic heating and stagnant meteorological conditions that restrict vertical mixing
290 ([Zhong et al., 2018](#)). In contrast, summer exhibited the lowest extinction coefficients at 532 nm across the profile,
291 suggesting the effective dispersion of aerosols due to strong convection and a high planetary boundary layer ([Li et](#)
292 [al., 2015](#)). Spring and autumn showed intermediate levels. The most significant differences between seasons appeared
293 below 1 km, especially in the 0.2–0.6 km range ([Zhong et al., 2018](#)). Above 1.0 km, the extinction values in all
294 seasons converged toward high altitude, indicating a reduced aerosol presence in the upper layer ([Liu et al., 2024](#)).

295 The depolarization ratio also exhibited seasonal differences (**Fig. 4b**). With increasing altitude, the contribution
296 of non-spherical particles increases, leading to a steady rise in depolarization ratio. This is attributed to the fact that
297 non-spherical particles exhibit stronger anisotropic light scattering than nearly spherical fine-mode aerosols that
298 dominate near the surface ([Wang et al., 2020b](#)). In the lower layer below 0.6 km, spring showed the highest
299 depolarization ratios, which were attributed to a greater proportion of non-spherical particles such as mineral dust or
300 internally mixed soot ([Biuki et al., 2022](#)). This may result from springtime dust resuspension and aged industrial
301 emissions. In contrast, summer had the lowest depolarization ratios, implying that aerosols were dominated by more
302 spherical particles, such as those formed through secondary processes (e.g., sulfate or organic aerosols) ([Sun et al.,](#)
303 [2013](#)). In autumn and winter, values were moderate and stayed between the two extremes. However, the seasonal
304 pattern changed above 0.6 km. Winter showed the highest depolarization ratio, while spring became the lowest. The
305 vertical profile revealed that the change in particle shape with height strongly depends on seasons ([Wang et al., 2004](#)).
306 In winter, the low ambient temperatures in the upper atmosphere promote the formation of non-spherical particles
307 (e.g., ice crystals and irregular aerosols), which substantially enhance the depolarization ratio due to their anisotropic
308 light-scattering properties ([Haarig et al., 2017](#); [Wang et al., 2021](#); [Yu et al., 2021](#)). In addition, elevated aerosol layers
309 were dominated by long-range transported dust with pronounced nonspherical properties. However, aerosols in the
310 upper layer were more spherical and less influenced by dust in spring ([Wang et al., 2020b](#)).

311

312



313

314 **Figure 4.** Seasonal variation of vertical aerosol (a) extinction coefficient and (b) depolarization profiles at 532 nm
 315 from LiDAR measurements. The whiskers represent the 90th and 10th percentiles, respectively. The shaded areas
 316 represent the 25th-75th percentiles. The connected lines depict the trend of mean values across different heights.

317

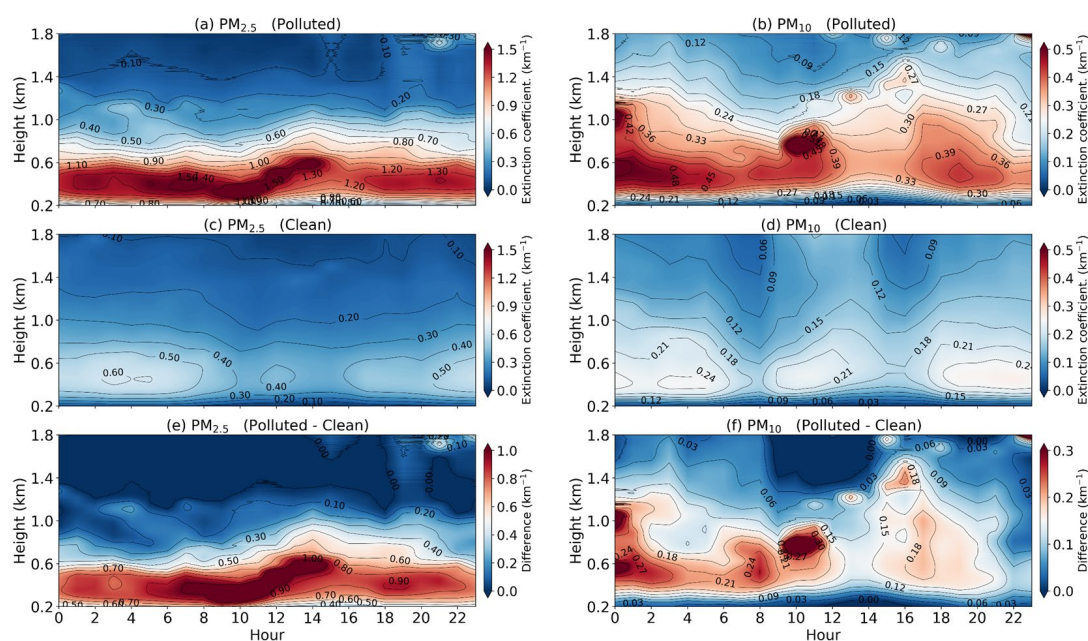
318 The extinction coefficient is significantly higher on $\text{PM}_{2.5}$ -polluted days than on PM_{10} polluted days. This is
 319 attributed to the optimal size match between fine-mode particles ($\leq 2.5 \mu\text{m}$) and visible light ($0.4\text{--}0.7 \mu\text{m}$), as well
 320 as their chemical components, which are more efficient at scattering and absorbing light (Wang et al., 2021; Chen et
 321 al., 2023). The extinction coefficients at 535 nm exhibited clear differences between polluted and clean days for both
 322 $\text{PM}_{2.5}$ and PM_{10} , with strong vertical and diurnal variation (Fig. 5). For $\text{PM}_{2.5}$, polluted days were characterized by
 323 significantly higher extinction values below 0.9 km, especially during the nighttime and the period from early
 324 morning to near noon (Wang et al., 2024). This enhancement was mainly attributed to the stable boundary layer and
 325 limited vertical mixing during the night, which favored the accumulation of aerosols near the surface. Strong solar
 326 radiation enhances photochemical reactions, leading to substantial secondary aerosol formation at noon and a lift in
 327 altitude (Fig. 5a). However, extinction values near the surface (below 0.4 km) were relatively low during 12:00-15:00
 328 (BJT), with high values concentrated mainly around 0.6 km. This midday vertical uplift of the aerosol layer
 329 corresponds to the decrease in near-surface $\text{PM}_{2.5}$ shown in Fig. 3, as enhanced convective mixing lifts fine particles

330 upward and weakens near-surface extinction. Hence, strong daytime turbulence promotes the vertical transport of
331 aerosols, resulting in an elevated and vertically expanded aerosol layer (**Fig. 5a**) ([Wang et al., 2024](#)). During this
332 period (12:00–15:00 BJT), the enhanced extinction was concentrated around 0.6 km, extending vertically from the
333 surface to this altitude, rather than peaking near the ground. The upward expansion of aerosols was driven by
334 boundary layer development and persistent emission sources ([Dai et al., 2020](#)). In contrast, clean days showed low
335 extinction values throughout the day, with little vertical variation and no significant peak. For PM₁₀, extinction
336 coefficients at 532 nm were also increased on polluted days (**Fig. 5b**). However, the enhancement of extinction values
337 extended to a higher altitude compared to that of PM_{2.5}, reaching up to 1.2 km. The primary increase occurred during
338 the night and early morning, with a minor secondary rise observed around midday. ([Li et al., 2020](#)). Clean-day
339 extinction remained uniformly low with minimal temporal variation (**Fig. 5d**).

340 For the depolarization ratio, distinct patterns also emerged between polluted and clean days for both PM_{2.5} and
341 PM₁₀ (**Fig. 6**). For PM_{2.5}, depolarization ratios near the surface (below ~0.6 km) were relatively low on polluted days,
342 particularly during nighttime and early morning (**Fig. 6a**). This can be attributed to the accumulation of fine, spherical
343 particles in the stable boundary layer, which tend to have lower depolarization ratios. As altitude increased,
344 depolarization ratios rose. This indicates the presence of more irregularly shaped or coarser particles aloft, possibly
345 from transported dust or aged aerosols. In contrast, clean days showed uniformly low depolarization ratios across
346 most heights, consistent with the dominance of fine, spherical aerosols under favorable dispersion conditions (**Fig.**
347 **6c**). For PM₁₀, depolarization ratios at 532 nm on polluted days exhibited a different behavior (**Fig. 6b**). Starting
348 around 8:00 (BJT), elevated depolarization values were observed across a broad vertical layer, extending up to ~1.2
349 km throughout the day. This suggests that coarser particles, which typically have higher depolarization ratios, were
350 more effectively mixed vertically and persisted at higher altitudes compared to PM_{2.5}. The broader vertical
351 distribution of PM₁₀ depolarization signals reflects the larger size and potentially different sources (e.g., resuspended
352 dust, industrial emissions) of these particles, which are less confined by boundary layer dynamics than finer PM_{2.5}.
353 The increased depolarization ratio at noon during PM₁₀-polluted days is attributed to midday boundary layer growth
354 and frontal dust transport, elevating non-spherical coarse particle concentrations.

355 The difference between polluted and clean days highlighted a strong increase in near-surface extinction during
356 early morning on polluted days, indicating suppressed vertical mixing and increased emission accumulation (**Fig.**
357 **5e&f**). For PM_{2.5}, the differences were concentrated near the ground, especially below 0.9 km. The strongest
358 enhancement appeared between 7:00 and 14:00 (BJT). A subtle lifting with height was observed around midday.
359 Noon solar radiation maximizes surface heating, which causes severe thermal convection. The lower atmosphere

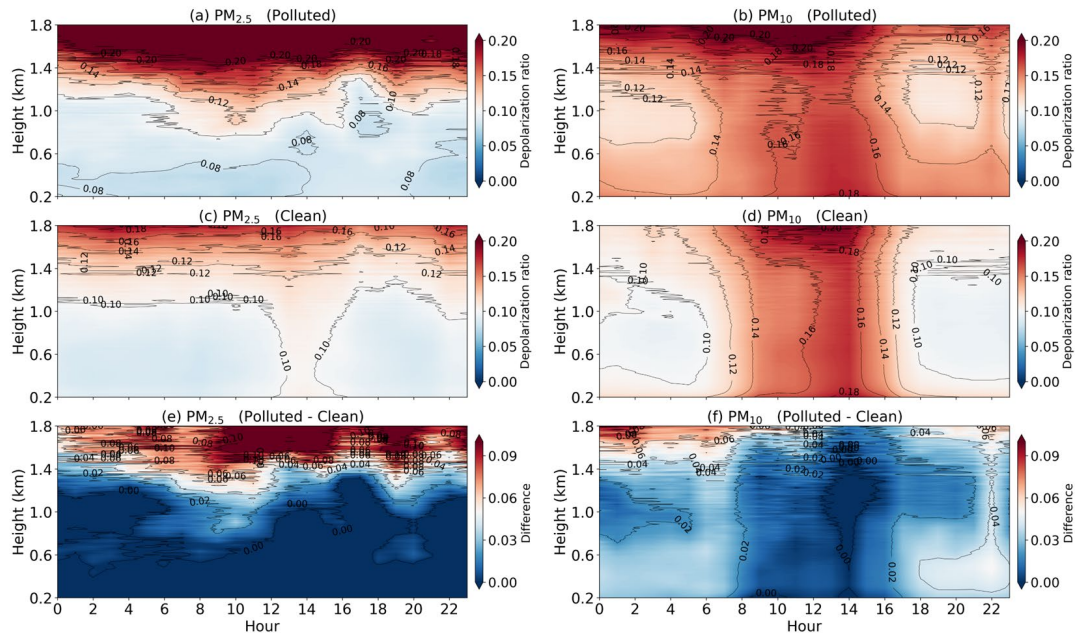
360 becomes unstable as a result of the hot Earth transferring energy upward. It could break the stable stratification and
 361 drive upward air motion. Pollutants trapped near the surface are lifted, reducing extinction in the lower layer (<0.4
 362 km) while increasing it aloft as vertical mixing intensifies (Wang et al., 2024). For PM₁₀, the enhancement tended to
 363 be localized and less vertically extended. The coarse particles may be lifted in upstream source regions, but their
 364 vertical transport weakens significantly along the trajectory. As a result, the transport altitude of PM₁₀ reaching Hefei
 365 was largely confined below 1.2 km (Shim et al., 2022). Compared to PM_{2.5}, the high-value region for PM₁₀ on polluted
 366 days has a higher vertical extension, and the period of strong extinction is shorter. The particles of PM₁₀ are relatively
 367 large and heavy, which leads to rapid sedimentation and thus a short duration of heavy pollution. Pollutants tend to
 368 accumulate in the middle and low altitudes (0.4-1.2 km) on polluted days.



369

370 **Figure 5.** Diurnal variation in the vertical distribution of aerosol extinction coefficient (Winter days for PM_{2.5}: First
 371 column; Spring days for PM₁₀: Second column) under days with (a, b) polluted, (c, d) clean, and (e, f) the difference
 372 between the two. All data are presented in Beijing time (BJT = UTC + 8 h) for the 532 nm channel.

373



374

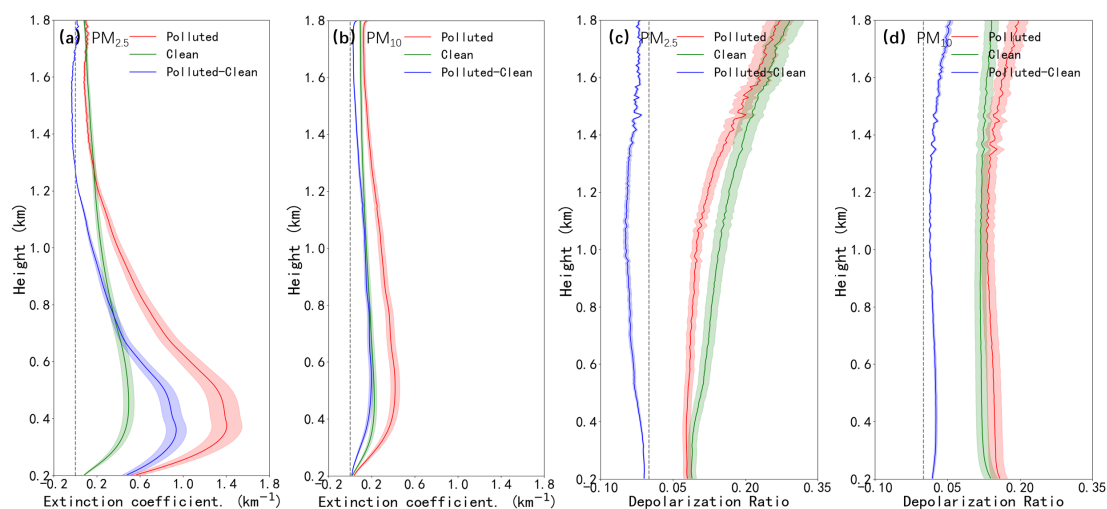
375 **Figure 6.** Same as Fig. 5, but for depolarization ratio.

376

377 To further analyze the vertical aerosol properties under different pollution levels, the mean extinction coefficient
 378 and depolarization ratio at 532 nm were calculated across three representative conditions (**Fig. 7**). Unlike the temporal
 379 variation that emphasized vertical profile distributions (**Fig. 5&6**), these curves highlight altitude-related trends (e.g.,
 380 gradual changes, peak positions, and inflection points) for the comparison between polluted, clean, and difference
 381 conditions. For $PM_{2.5}$, the extinction coefficient decreased exponentially with height and intensified sharply below
 382 0.4 km on polluted days (**Fig. 7a**) ([Wang et al., 2020a](#)). The near-surface value reached up to 1.4 km^{-1} at 0.4 km,
 383 which was nearly three times higher than that on clean days. The difference was most significant within the boundary
 384 layer, especially between 0.3-0.6 km. For PM_{10} (**Fig. 7b**), although the overall extinction values were lower than
 385 those of $PM_{2.5}$, the difference between polluted and clean days remained obvious. The polluted-clean difference for
 386 PM_{10} was more confined below 1.2 km. This discrepancy may be attributed to that the coarse-mode particles tend to
 387 concentrate closer to the surface due to their limited vertical transport.

388 The vertical distributions of the depolarization ratio under different pollution levels are presented in **Figs. 7**
 389 **(c&d)** for $PM_{2.5}$ and PM_{10} , respectively. For $PM_{2.5}$, the depolarization ratio on clean days was higher than that on
 390 polluted days across the entire vertical column up to 1.8 km (**Fig. 7c**). The depolarization ratio of $PM_{2.5}$ increases
 391 with height. The most significant difference in depolarization ratios between polluted and clean days was observed
 392 around 1 km. Above this height, the difference narrowed but clean days still showed slightly higher values. Unlike
 393 near-surface $PM_{2.5}$, which is dominated by local pollution sources, $PM_{2.5}$ at higher altitudes is mainly associated with

394 long-range transport in the free troposphere, leading to higher depolarization ratios. Higher altitudes have more PM_{2.5}
 395 particles from long-range transport in the free troposphere, which possess higher depolarization ratios (Vakkari et al.,
 396 2021; Wang et al., 2021). Even at higher altitudes, the residual influence of cleaner, non-spherical particle sources in
 397 the background air kept the clean-day depolarization ratio higher (Li et al., 2020). For PM₁₀, the depolarization ratio
 398 of polluted days was higher than that of clean days across the entire vertical range (Fig. 7d), reflecting a greater
 399 abundance of coarse-mode and irregularly shaped particles on polluted days. Below 1.2 km, the depolarization ratio
 400 of PM₁₀ was distinctly higher than that of PM_{2.5} on polluted days. This difference emphasized the dominant influence
 401 of coarse, non-spherical particles (e.g., dust and mechanically suspended material) in the PM₁₀ fraction, particularly
 402 near the surface (Shim et al., 2022). On PM₁₀-polluted days in autumn, the depolarization ratio increased with height,
 403 which is mainly also affected by the long-distance transport of dust in the free troposphere.
 404

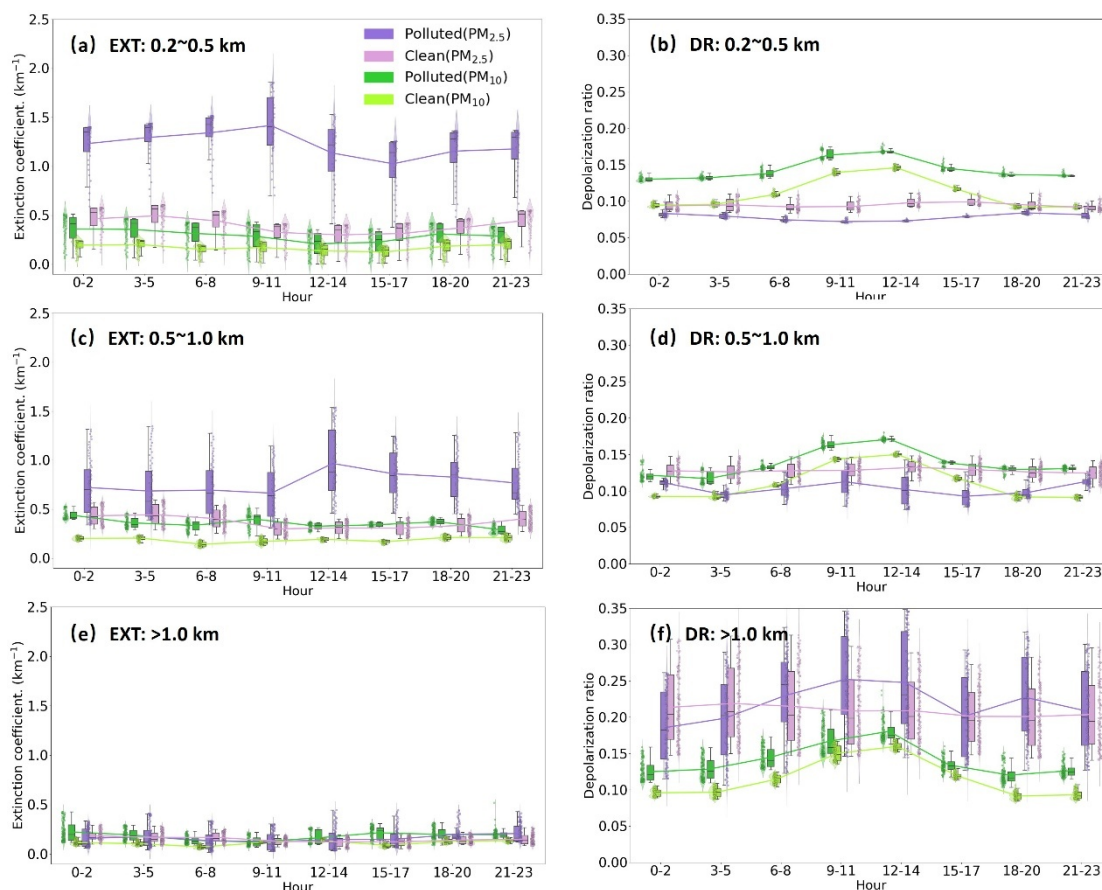


405
 406 **Figure 7.** Vertical profiles of aerosol (a, b) extinction coefficient and (c, d) depolarization ratio at 532 nm for (a, c)
 407 PM_{2.5} in winter and (b, d) PM₁₀ in spring on polluted, clean days, and the difference between the two. The gray
 408 dashed line represents the zero line. Note: The extinction coefficient and depolarization ratio of individual polluted
 409 and clean days are positive physical quantities. Negative values in the "Polluted-Clean" panels indicate that the
 410 aerosol optical parameters (extinction coefficient or depolarization ratio) are higher on clean days than on polluted
 411 days. All data are presented in Beijing time (BJT = UTC + 8 h) for the 532 nm channel.

412
 413 **Figure 8** presents the 3-hourly variation of extinction coefficient and depolarization ratio at 532 nm on polluted
 414 and clean days across three altitude layers (0-0.5 km, 0.5-1 km, and 1-1.8 km). Below 0.5 km, the extinction
 415 coefficients were markedly higher on polluted days for PM_{2.5} than that on clean days, with peak values occurring at
 416 03:00-12:00 (BJT) (Fig. 8a), which was consistent with the variation in surface pollutant concentrations (Fig. 3). The

417 depolarization ratio for $PM_{2.5}$ was lower on polluted days in contrast with clean days. This is due to the dominance
418 of spherical fine particles (e.g., sulfates, organic aerosols) from anthropogenic and secondary sources (**Fig. 8a&c**).
419 These particles scatter light less directionally compared to the irregular coarse particles (e.g., dust) prevalent on clean
420 days. In contrast, both the extinction coefficient and depolarization ratio for PM_{10} were high on polluted days ([Zhang
421 et al., 2020a](#)). At the layer between 0.5 and 1 km, the extinction coefficient for $PM_{2.5}$ showed a significant peak
422 around 12:00 to 15:00 (BJT) on polluted days, which was consistent with the upward transport of pollutants to around
423 0.6 km during the same period as shown in the diurnal vertical structure (**Fig. 5**). The extinction values decreased
424 significantly and remained at low levels above 1 km (**Fig. 8e**). However, the depolarization ratio remained relatively
425 high during polluted periods. The depolarization ratio for on days in winter was higher than that of spring, mainly
426 because $PM_{2.5}$ pollution contains a higher proportion of irregular particles from coal-fired fly ash and industrial
427 emissions (**Fig. 8f**). The low temperatures inhibit the diffusion and settlement of coarse particles. In contrast, days in
428 spring for PM_{10} pollution were more affected by coarse particles such as windblown dust. Although these particles
429 are irregular in shape, their large particle size makes them prone to settling. Moreover, the strong atmospheric fluidity
430 in spring led to a slightly lower depolarization ratio compared to winter. Overall, the greatest contrast between
431 polluted and clean days was observed in the lowest layer, where both particle concentration and shape varied most
432 distinctly with pollution level and time of day ([Zhong et al., 2018](#)).

433



434

435 **Figure 8.** Diurnal variations of (EXT: a, c, e) extinction coefficient and (DR: b, d, f) depolarization ratio at 532 nm
 436 on polluted and clean days for PM_{2.5} and PM₁₀ at (a, b) 0.2-0.5 km, (c, d) 0.5-1.0km, and (e, f) above 1.0 km,
 437 respectively. The whiskers represent the 90th and 10th percentiles, respectively. The shaded areas represent the 25th-
 438 75th percentiles. The connected lines depict the trend of mean values across different heights. All data are presented
 439 in Beijing time (BJT = UTC + 8 h) for the 532 nm channel.

440

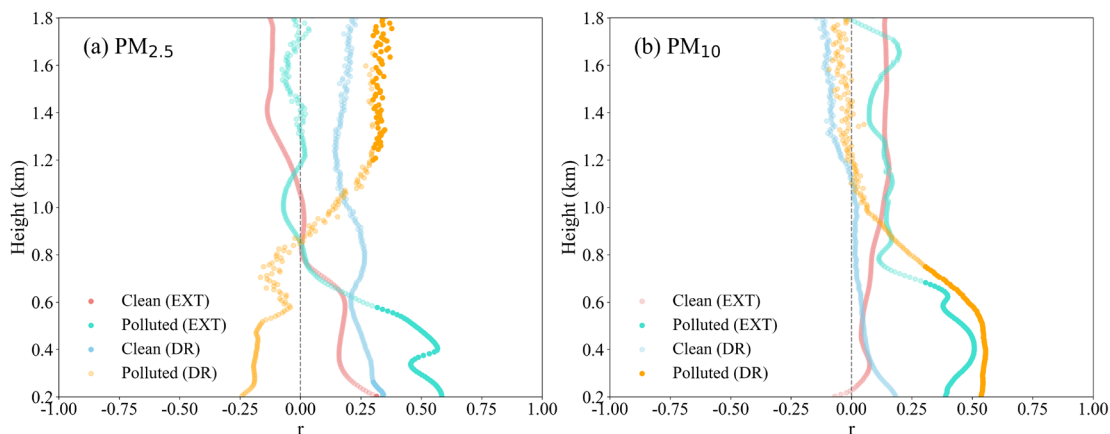
441 3.3 Role of aerosol extinction coefficient and depolarization ratio at different altitudes on 442 ground-based PM_{2.5} and PM₁₀ concentrations

443 **Figure 9** shows the vertical profiles of the relationships between surface pollutant concentrations and aerosol
 444 optical properties (extinction coefficient and depolarization ratio at 532 nm) on polluted and clean days. For PM_{2.5},
 445 the extinction coefficients showed a clear positive correlation with surface PM_{2.5} concentration throughout the profile
 446 below 0.9 km on polluted days, marking a key boundary for vertical variation in particle composition (**Fig. 9a**). The
 447 values on polluted days increase sharply near the surface, suggesting a local accumulation. A negative correlation
 448 was observed between the depolarization ratio and PM_{2.5} concentration below 0.9 km on polluted days, as elevated
 449 PM_{2.5} levels corresponded to a higher fraction of fine, spherical particles with low depolarization ([Zhang et al., 2020a](#)).

450 In contrast, clean days showed a consistently positive correlation between depolarization ratio and surface pollutants
 451 throughout the vertical profile.

452 The increased depolarization levels are linked to greater proportions of non-spherical particles, such as dust or
 453 mechanically suspended matter (Vakkari et al., 2021). The depolarization ratio showed consistently positive
 454 correlations with surface PM₁₀ concentration on polluted days, especially below 1.2 km (Fig. 9b). On clean days, the
 455 correlation between the depolarization ratio and PM₁₀ concentration remained near zero, reinforcing that the
 456 depolarization ratio is a distinguishing feature of coarse-mode aerosols. These results revealed the contrasting aerosol
 457 properties between PM_{2.5} and PM₁₀ pollution. PM_{2.5} events were dominated by fine, spherical particles that reduce
 458 depolarization, while PM₁₀ events were closely associated with the presence of coarse, non-spherical particles that
 459 enhanced depolarization signals (Biuki et al., 2022).

460



461

462 **Figure 9.** Vertical distributions of correlation (r) between aerosol optical properties (532 nm) and ground-based
 463 pollutants (a: PM_{2.5} in winter, b: PM₁₀ in spring) on clean and polluted days. EXT = extinction coefficient; DR =
 464 depolarization ratio. The gray dashed line represents the zero line.

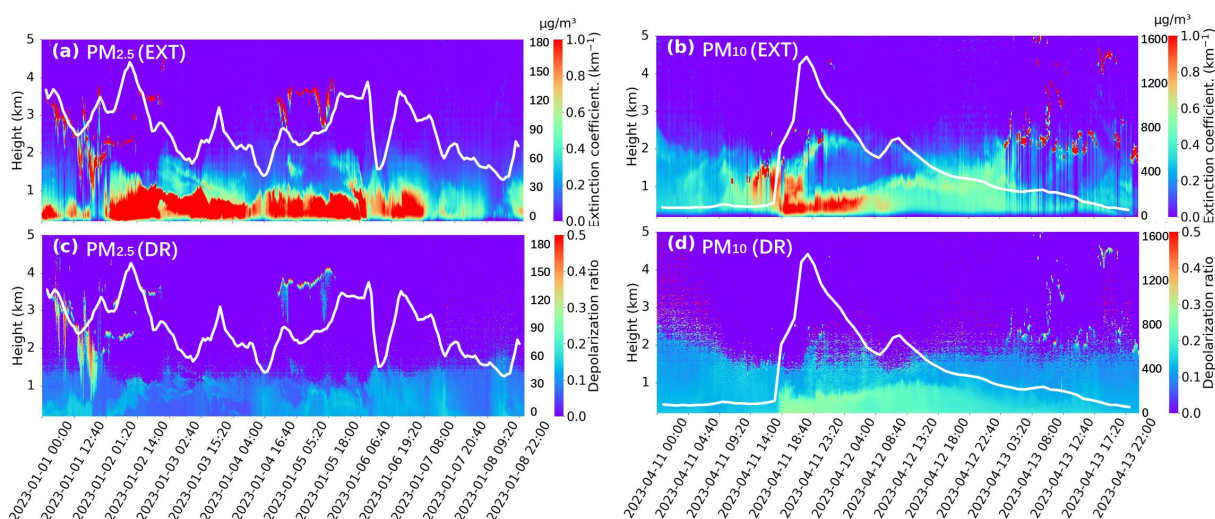
465

466 3.4 Analysis of LiDAR observations during heavy pollution episodes

467 Temporal variations of the extinction coefficient and depolarization ratio at 532 nm exhibited a clear association
 468 with PM_{2.5} and PM₁₀ concentrations, effectively highlighting severe pollution periods (Fig. 10). Severe PM_{2.5}
 469 pollution was evident at 10:00 on January 2, 2023 (BJT), with the maximum hourly concentration reaching 159.6
 470 $\mu\text{g}/\text{m}^3$. The peak of the extinction coefficient matched the actual maximum concentration of PM_{2.5}, with fine
 471 particulate matter exhibiting strong light-scattering properties at this time (Fig. 10a). However, the depolarization
 472 ratio of PM_{2.5}-polluted days was markedly decreased during this peak period (Fig. 10c). Physically, the extinction
 473 coefficient scales with aerosol concentration and size, while the depolarization ratio is governed by particle

474 morphology. Spherical fine particles such as hygroscopic sulfates and nitrates dominating this $PM_{2.5}$ event, leading
 475 to increased extinction and decreased depolarization. A dramatic peak in PM_{10} concentration was observed, with the
 476 highest hourly value of $1440 \mu\text{g}/\text{m}^3$ recorded at 22:00 p.m. (BJT) on April 11, 2023. The severe PM_{10} event was
 477 reflected by a pronounced increase in the extinction coefficient (**Fig. 10b**) ([Sun et al., 2013](#)). In addition, the
 478 depolarization ratio exhibited high values during this period, which aligned with the elevated extinction coefficient
 479 and was consistent with the irregular morphology of coarse particles that contributed to both stronger light scattering
 480 and greater depolarization (**Fig. 10d**). Overall, the profiles of the extinction coefficient and depolarization ratio
 481 correspond directly to the temporal patterns of $PM_{2.5}$ (January 1–8, 2023) and PM_{10} (April 11–13, 2023)
 482 concentrations (**Fig. 10**). Peaks in pollutant concentrations were reflected in enhanced extinction coefficients and
 483 characteristic depolarization ratio patterns ([Zhong et al., 2018](#)). This confirms that these optical metrics effectively
 484 identify severe pollution episodes.

485



486

487 **Figure 10.** Pollution Episodes: Temporal dynamics of (a, b) extinction and (c, d) depolarization parameters for the
 488 532 nm channel during severe (a, c) $PM_{2.5}$ (January 1–8, 2023) and (b, d) PM_{10} (April 11–13, 2023) periods in Hefei.
 489 The white lines represent the hourly (a) $PM_{2.5}$ and (b) PM_{10} concentrations, with their scale on the secondary y-axis.
 490 All data are presented in Beijing time (BJT = UTC + 8 h). EXT = extinction coefficient; DR = depolarization ratio.

491

492 3.5 Analysis of meteorological conditions and their driving role in air pollution

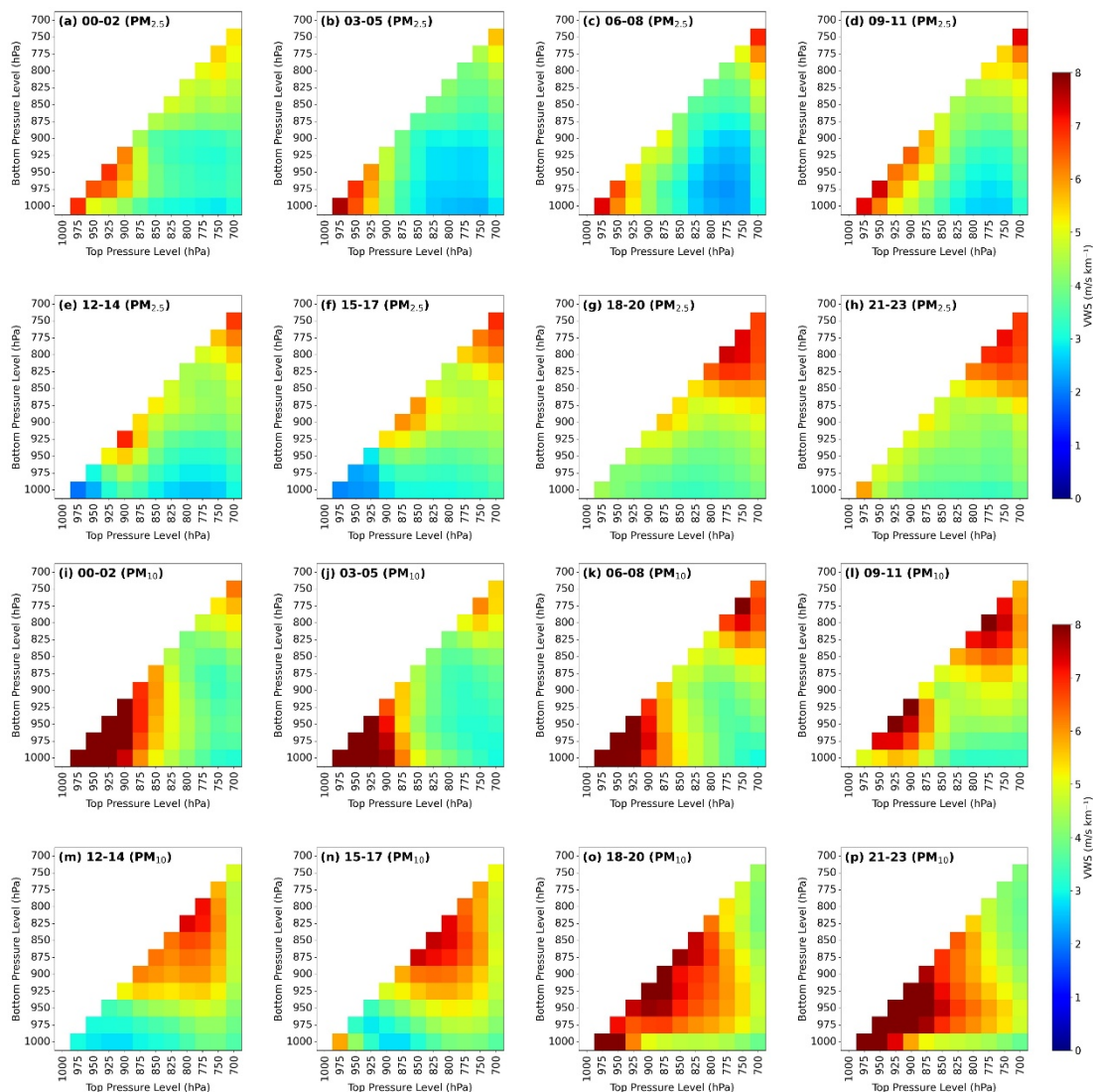
493 **Figure S1** shows boxplots of the concentrations of $PM_{2.5}$ and PM_{10} in temperature (T), relative humidity (RH),
 494 surface pressure (PRS), and wind speed (WS) bins, respectively. Overall, the relationships of temperature with $PM_{2.5}$,
 495 PM_{10} were not significant (**Fig. S1a&e**). The RH exerted distinct influences on PM_{10} and $PM_{2.5}$ concentrations (**Fig.**
 496 **S1b&f**). Higher $PM_{2.5}$ concentrations were associated with increased RH, primarily due to elevated humidity

497 promoting the condensation of gaseous precursors (e.g., sulfur dioxide, nitrogen oxides) onto pre-existing PM_{2.5}
498 particles (**Fig. S1b**) ([Wang et al., 2004](#)). Additionally, it accelerated secondary aerosol formation via aqueous-phase
499 chemical reactions in the atmosphere, thereby elevating PM_{2.5} levels ([Yang et al., 2022](#)). In contrast to PM_{2.5}, the
500 relationship between PM₁₀ concentrations and RH was inverse (**Fig. S1f**). Higher RH promotes moisture uptake
501 and growth of coarse PM₁₀ particles, accelerating their sedimentation and wet deposition, thereby reducing ambient
502 concentrations ([Gao et al., 2020](#); [Ma et al., 2023](#)). PRS tended to increase with rising concentrations of PM_{2.5} and
503 PM₁₀ (**Fig. S1c&g**). The average pressure values were lower on clean days (PM_{2.5} ≤ 75 μg/m³, PM₁₀ ≤ 150 μg/m³)
504 and became higher on polluted days. The high-pressure systems promote atmospheric stability and suppress vertical
505 mixing, thereby facilitating the accumulation of particulate matter near the surface ([Li et al., 2015](#)). Wind speed
506 exhibited a decreasing trend with increasing PM_{2.5} concentrations (**Fig. S1d&h**). Lower wind speeds during heavy
507 pollution periods indicate weak horizontal dispersion, which contributes to the persistence and accumulation of fine
508 particles in the boundary layer. In addition, the polar plot of PM_{2.5} concentrations shows a directional pattern, with
509 the highest values predominantly associated with winds from the northwest (**Fig. S2a**). The cities of northern Anhui
510 Province, Henan Province, and even further north were characterized by dense industrial activities and frequent
511 wintertime heating emissions, which contribute to elevated PM_{2.5} levels ([Qian et al., 2024](#); [Shi et al., 2018](#)). For PM₁₀,
512 the concentration distribution was more spatially confined but still shows a dominant contribution from the northwest
513 area ([Huang et al., 2016](#)). The most intense PM₁₀ concentrations were clustered in the northwest, appearing localized
514 and patchy (**Fig. S2b**).

515 VWS is a key dynamic factor affecting pollutant dispersion, as it influences mechanical turbulence and vertical
516 mixing within the boundary layer ([Deng et al., 2023](#)). **Figures 11** and **12** illustrate the diurnal variation of VWS on
517 polluted and clean days, respectively. For PM_{2.5}, weak shear persisted throughout the boundary layer on polluted days
518 when temperature inversions and stable stratification typically dominate the lower atmosphere (**Fig. 11a-h**). Clean
519 days showed stronger shear during most periods, enhancing upward transport and dilution of fine particles (**Fig. 12**).
520 Notably, the difference in VWS between polluted and clean days was more pronounced in the lower boundary layer
521 (1000–900 hPa) than in the upper boundary layer (875–700 hPa) ([Zhang et al., 2020b](#)). Hence, suppressed vertical
522 mixing near the surface contributed significantly to the accumulation of PM_{2.5}. Surface air quality tends to deteriorate
523 significantly due to pollutant accumulation near the ground, especially in cases where shear is insufficient in the
524 lower layer ([Wang et al., 2024](#)), which was consistent with the trend that the extinction coefficient at 532 nm near the
525 surface is higher than that in the upper layer (**Figs. 7 & 8**).

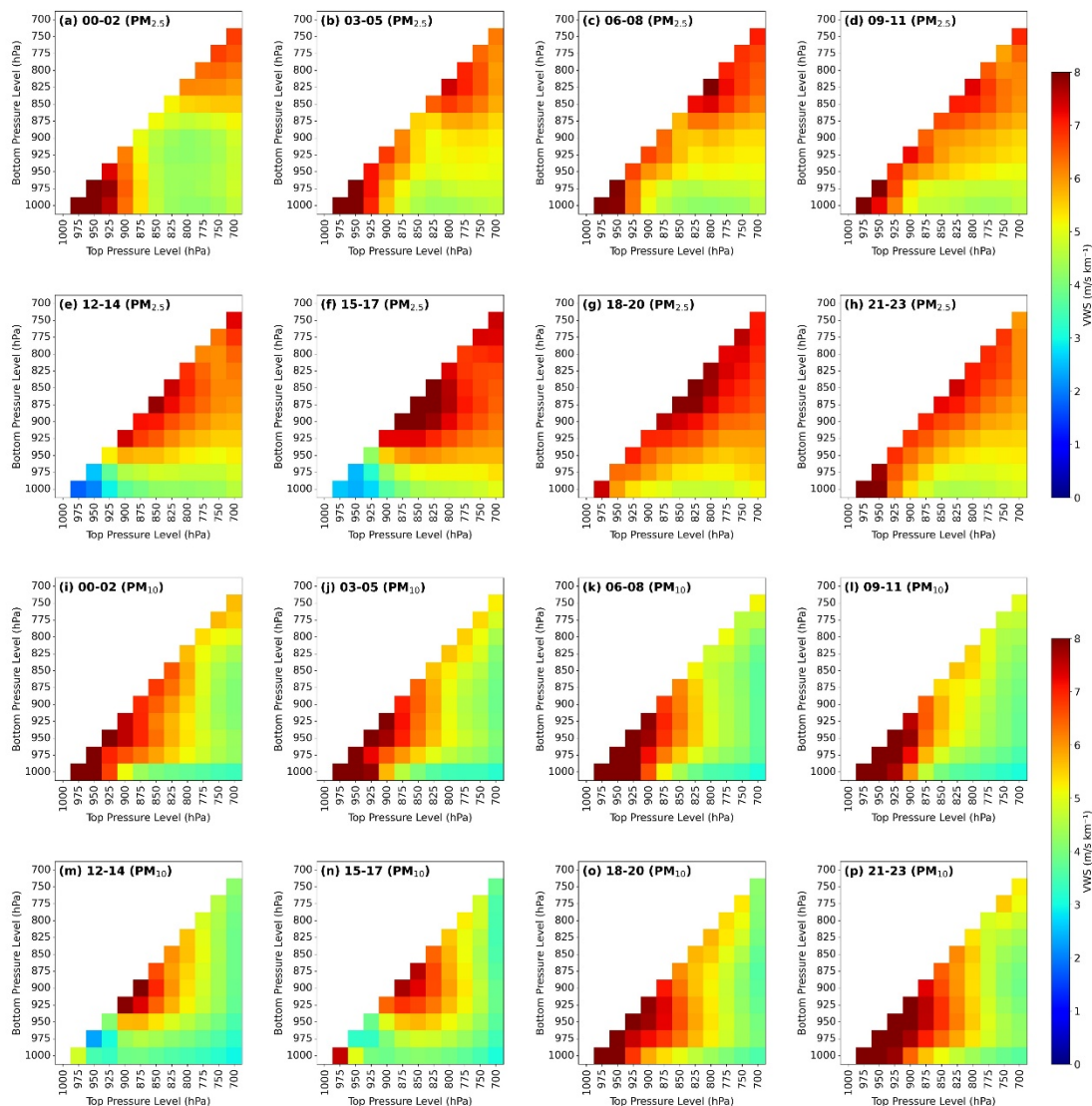
526 Contrary to the expectation that polluted days generally exhibited weak VWS, the VWS associated with PM₁₀

527 on polluted days was not consistently lower than that on clean days (**Fig. 11 i-p, Fig. 12 i-p**). In particular, dust storms
528 with high PM_{10} levels are typically accompanied by intensified VWS, which is conducive to dust uplift and transport
529 under dynamic atmospheric conditions ([Yang et al., 2019](#)). The large VWS associated with PM_{10} would clear the air
530 in the upper air at the beginning but later contributed to raising surface PM_{10} levels through regional transport at the
531 near-surface and through downward transport of aerosol particles from the upper air. During the onset phase of dust
532 intrusion, intensified shear facilitates both horizontal and vertical transport of dust particles ([Biuki et al., 2022](#)). From
533 00:00 to 11:00 (BJT), the VWS in the upper layer (850 hPa-700 hPa) gradually increases on $PM_{2.5}$ -polluted days. At
534 night, the near-surface air cools, forming a stable temperature inversion layer that inhibits vertical mixing. Hence,
535 the stable structure would lead to weak VWS in the upper layer. As the sun rises in the mornings, the inversion layer
536 gradually dissipates, and vertical mixing shifts from being suppressed to active (**Fig. 11 i-l**). The VWS in the upper
537 layer gradually increases due to the mixing effect. In addition, PM_{10} pollution often occurs during cold front passage.
538 The vertical gradient of wind direction and speed changes suddenly near the frontal surface when cold and warm air
539 masses converge. Once the front is located in a certain pressure range, the wind shear may be significantly higher
540 than that in the surrounding layers. The weaker VWS between adjacent pressure layers (e.g., near 825–850 hPa) may
541 correspond to the fault distribution (**Fig. 11 i-l**). The sinking of cold air also leads to an increase in VWS at the lower
542 level.



543

544 **Figure 11.** Three-hourly variation of vertical wind shear for (a-h) $PM_{2.5}$ and (i-p) PM_{10} on polluted days in Hefei at
 545 (a&i) 00:00–02:00 BJT, (b&j) 03:00–05:00 BJT, (c&k) 06:00–08:00 BJT, (d&l) 09:00–11:00 BJT, (e&m) 12:00–
 546 14:00 BJT, (f&n) 15:00–17:00 BJT, (g&o) 18:00–20:00 BJT, and (h&p) 21:00–23:00 BJT. Beijing Time (BJT) is
 547 UTC+8, the local standard time used in this study. The axes indicate the vertical bounds (upper and lower pressure
 548 levels) used to compute VWS, where the main diagonal (from top-right to bottom-left) corresponds to self-referential
 549 values for single-layer calculations. The color gradient represents the magnitude of VWS between adjacent
 550 atmospheric layers.



551

552 **Figure 12.** Same as Fig. 11, but under clean days.

553

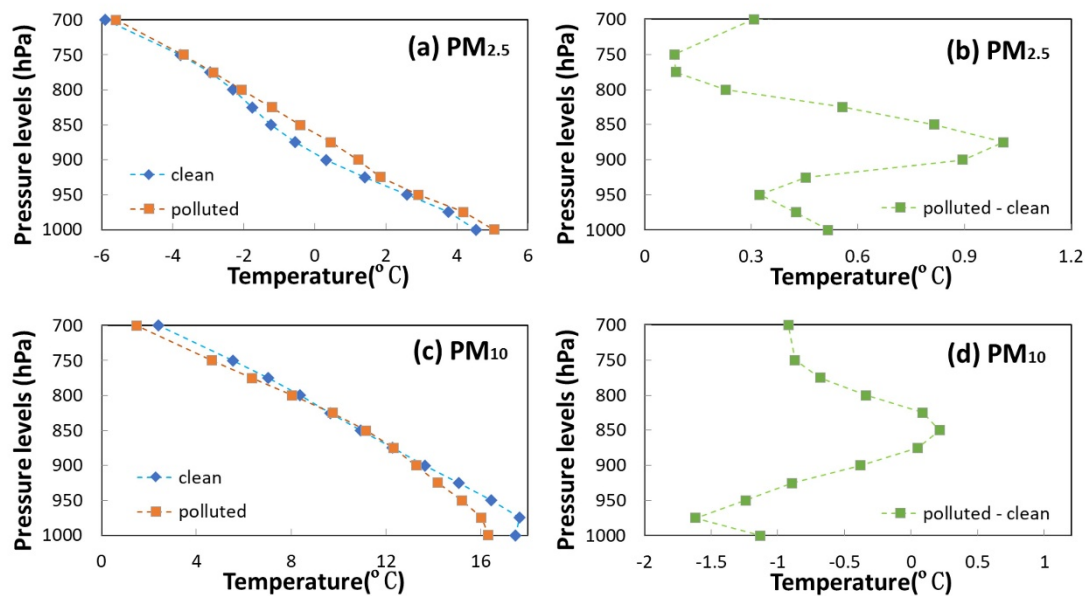
554 To clarify the synoptic influences on $PM_{2.5}$ and PM_{10} pollution, we analyzed the distributions of air temperature
 555 across different pressure levels from March 2021 to May 2023. During $PM_{2.5}$ pollution days, temperatures at all levels
 556 were consistently higher than those on clean days. The warming showed a notable pattern, with the most pronounced
 557 trend initially observed at 875 hPa, (**Fig. 13b**). The enhanced upper-level warming relative to the lower-level led to
 558 a thermally stable stratification, which inhibited vertical mixing and promoted the accumulation of $PM_{2.5}$ near the
 559 surface. In contrast, PM_{10} -polluted days exhibited negative temperature differences below 875 hPa (**Fig. 13d**),
 560 indicating the intrusion of cold air masses. These cold air masses, often accompanied by long-range dust transport,
 561 not only bring in PM_{10} particles from upwind regions but also suppress vertical mixing in the lower atmosphere due
 562 to their higher density. Notably, the altitude of the cooling (875 hPa) coincided with the effective aerosol layer height
 563 identified in our LiDAR-based analyses (**Figs. 8, 11, 12**), which supported the conclusion that dust particles were

564 primarily transported within this level.

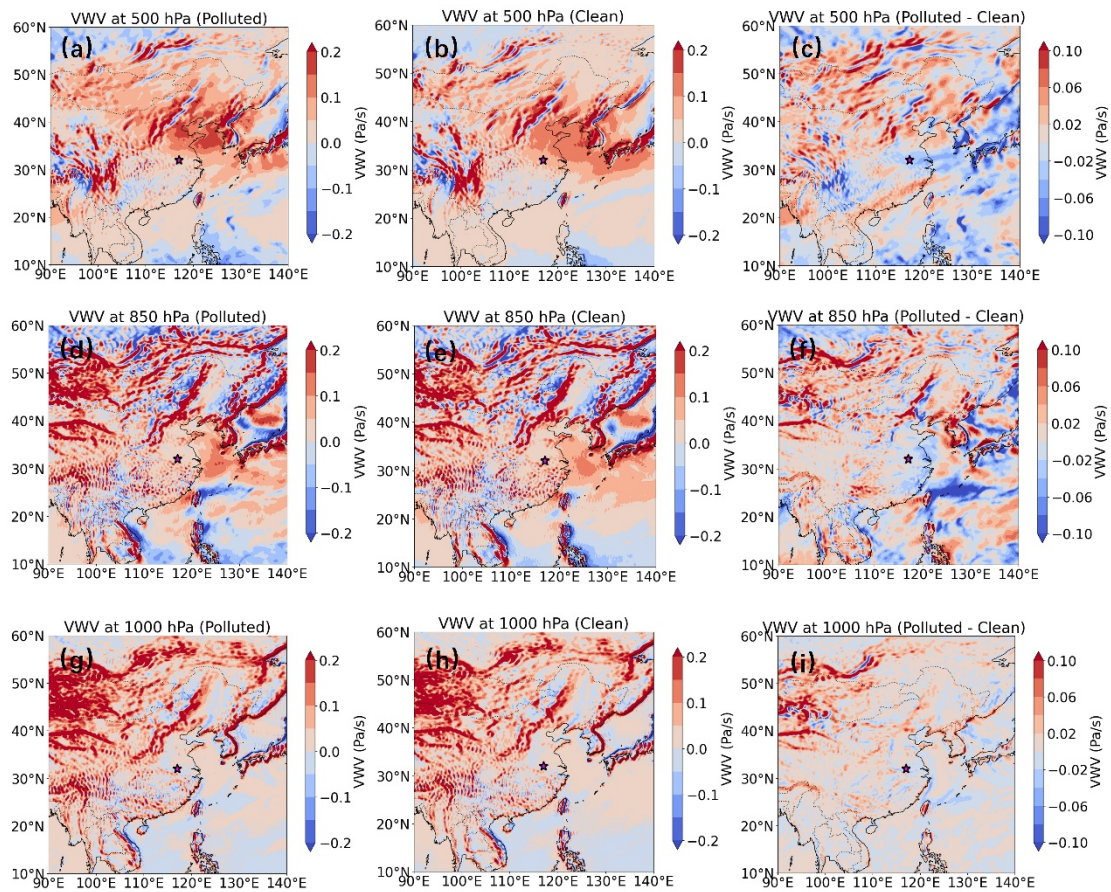
565 To further investigate the vertical thermal and humidity differences between clean and polluted days, we focus
566 on three key pressure levels (1000, 850, and 500 hPa). During PM_{2.5}-polluted periods, the warming at 850 hPa was
567 greater than that near the surface at 1000 hPa in Hefei (**Fig. S3f&i**). This vertical temperature structure created a
568 pronounced inversion, which inhibited the vertical mixing and enhanced the atmospheric stability. The lower
569 troposphere also exhibited elevated relative humidity, particularly in Hefei and nearby regions. Elevated relative
570 humidity suppresses turbulent exchange and reduces dilution capacity, and hence forms a shallow, moist, and stable
571 boundary layer that favors pollutant persistence and contributes to poor air quality. In contrast, the clean days showed
572 a lower humidity in the boundary layer and a weaker vertical temperature gradient, allowing enhanced upward motion
573 and effective removal of surface aerosols ([Deng et al., 2023](#)). PM₁₀ pollution episodes occurred under a markedly
574 different meteorological background (**Fig. S4**). Specifically, the relative humidity at both 1000 hPa and 850 hPa was
575 significantly lower on PM₁₀-polluted days than on clean days (**Fig. S4f&i**). Aloft cold air intrusions occurred on PM₁₀
576 pollution days, creating favorable conditions for the large-scale transport of dust into Hefei. Under such dry and calm
577 conditions, the accumulation of PM₁₀ is likely driven by mechanical resuspension or regional dust transport rather
578 than secondary aerosol formation processes enhanced by moisture ([Li et al., 2020](#)). Overall, these findings reveal that
579 PM_{2.5} episodes over Hefei are typically governed by moist and thermodynamically stable boundary layers under
580 subsiding air masses, while PM₁₀ events are more influenced by dust-laden airflow and dry boundary-layer dynamics.
581 The distinct thermal and humidity structures observed across the vertical profile emphasize the importance of
582 differentiating pollution types when diagnosing meteorological drivers.

583 The vertical wind velocity was investigated at three pressure levels to reveal the dynamic mechanisms on PM_{2.5}
584 and PM₁₀ pollution days (**Figs. 14 & 15**). To better elucidate the meteorological characteristics between polluted and
585 clean conditions, we calculated the differences in vertical velocity between these two scenarios, as their broadly
586 similar large-scale background circulation patterns obscure the subtle but critical dynamic anomalies that drive
587 pollution formation. On PM_{2.5}-polluted days, the atmosphere around Hefei exhibits a clear subsidence trend at 850
588 and 1000 hPa (**Fig. 14**). The subsidence reflects the existence of high-pressure systems and stagnant synoptic
589 conditions, which contribute to the accumulation of fine particles. This inhibition of the upward motion of vertical
590 wind corresponds with a stable thermal structure, which can effectively restrict vertical exchange and compress the
591 boundary layer. During PM₁₀ pollution events, subsidence at 500 hPa is significantly stronger than that on clean days
592 (**Fig. 15**). However, Hefei is located in a unique region defined by upward motion at 850 hPa, with a comparable
593 weak upward movement also observed at 1000 hPa. The subsidence at 500 hPa stabilizes the atmosphere and

594 suppresses the upward dispersion of particles. Meanwhile, upward motion at 850 hPa and near the surface (1000 hPa)
 595 may be caused by local convergence or orographic lifting, allowing the uplift and recirculation of dust within the
 596 lower troposphere. This dynamic difference could reflect more complex interactions between local surface sources
 597 and large-scale synoptic. Upward motion at 850 hPa supports the interpretation that PM_{10} events are influenced by
 598 weak convective movements or vertical recycling of particles within a confined layer rather than stagnation alone.
 599 These findings reveal that $PM_{2.5}$ and PM_{10} pollution in Hefei are governed by contrasting vertical dynamic regimes.
 600 $PM_{2.5}$ events are closely tied to a uniformly subsiding atmosphere, which favors the trapping and accumulation of
 601 fine particles. In contrast, PM_{10} events are characterized by a layered structure, where upper-level subsidence and
 602 lower-level ascent work in tandem to recirculate coarse particles, rather than simply trapping them. This distinction
 603 underscores the need for targeted, pollutant-specific strategies in air quality forecasting and management.



604
 605 **Figure 13.** Vertical distributions of temperature for polluted, clean, and their difference in (a, b) $PM_{2.5}$ and (c, d)
 606 PM_{10} .



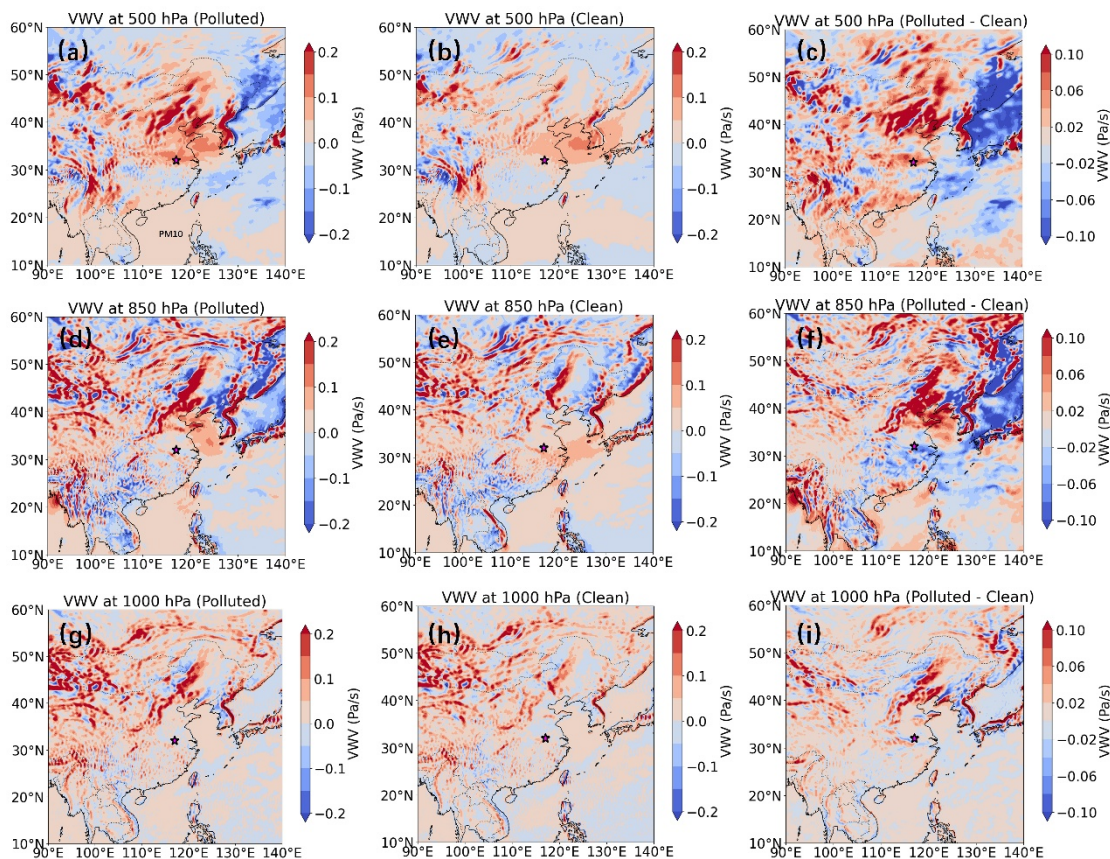
607

608 **Figure 14.** Spatial distribution of the vertical wind velocity (VWV) at three pressure levels (500 hPa: a–c;609 d–f; 1000 hPa: g–i) on PM_{2.5}-polluted (left column), clean (middle column) days and the difference between them

610 (right column), respectively. The areas highlighted with a red star represents the location of Hefei.

611

612



613

614 **Figure 15.** Same as Fig. 14, but on PM₁₀-polluted (left column), clean (middle column) days and the difference
 615 between them (right column), respectively.

616

617 4. Conclusions

618 This study comprehensively assesses the vertical structures of aerosols in Hefei by comparing fine (PM_{2.5}) and
 619 coarse (PM₁₀) particulate matter on clean and polluted days. We utilized long-term aerosol LiDAR measurements
 620 and reanalysis meteorological data to compare the vertical distribution characteristics of different particulate pollution
 621 types as well as the underlying thermodynamic and dynamic mechanisms that drive their vertical development.
 622 Aerosol extinction coefficients at 532 nm for PM_{2.5} and PM₁₀ were consistently higher on polluted days than on clean
 623 days. Since fine-mode particles predominate the aerosol population on PM_{2.5} pollution days, the depolarization ratios
 624 fell within a range lower than those observed on clean days. In contrast, PM₁₀-polluted days had larger depolarization
 625 ratios than clean days, indicating significant contributions from non-spherical coarse particles.

626 Our findings reveal that the accumulation of PM_{2.5} is closely linked to stable boundary layer structures
 627 characterized by high humidity, weak vertical shear, and a mid-level inversion temperature. These conditions
 628 collectively inhibit vertical exchange and confine fine particles near the surface. The vertical extinction and
 629 depolarization profiles support the dominance of aerosols during PM_{2.5} pollution, particularly in the lower 0.9 km. In

630 contrast, PM_{10} pollution is typically associated with low humidity and mechanically driven transport of dust from
631 upwind sources. The vertical profiles show enhanced depolarization ratios, indicating the presence of non-spherical,
632 coarse particles such as dust or resuspended material. Distinct vertical motion patterns identify the two types of
633 pollution. $PM_{2.5}$ episodes showed upward mobility in the mid-troposphere and near-surface subsidence, which
634 reinforced stratification and pollution trapping. However, PM_{10} events were distinguished by upper-level subsidence
635 coupled with low-level ascent, which might facilitate vertical transport of coarse particles during regional dust
636 episodes. These dynamic differences highlight that $PM_{2.5}$ and PM_{10} are generated by fundamentally separate
637 atmospheric processes, and a unified treatment of particulate pollution risks oversimplifies their behavior.

638 Expanding such analyses across multiple sites would also aid in identifying geographical heterogeneity and
639 testing the generalizability of the discovered trends. Future research may be directed toward integrating long-term,
640 high-resolution vertical observations with advanced modeling approaches to better understand the multiscale
641 dynamics behind various forms of particle pollution and create tailored mitigation solutions.

642

643 **Acknowledgments**

644 This work was supported by the Innovation and Development Special Project of Anhui Meteorological Bureau
645 (CXB202404), the Open Fund Project for Heavy Rain (BYKJ2025D03), the Science and Technology Projects of
646 Xizang Autonomous Region, China (XZ202502JD0041), the Special Project for Forecasters of Anhui Meteorological
647 Bureau (KY202003), and the 2025 Independent Innovation Scientific Research Project of Anhui Public
648 Meteorological Service Center (GFCX202504).

649

650 **Data Availability**

651 Hourly concentrations of major air pollutants were obtained from the China National Environmental Monitoring
652 Centre (CNEMC) (<https://www.cnemc.cn/>). Surface meteorological variables were obtained from the China
653 Meteorological Administration (CMA) (<http://data.cma.cn/en>). The ERA5 reanalysis dataset, used to investigate the
654 impact of synoptic systems on $PM_{2.5}$ and PM_{10} pollution, was freely accessible via the Copernicus Climate Change
655 Services platform (<https://cds.climate.copernicus.eu/datasets>).

656

657 **Author Contribution**

658 X.D. conceived the study; Y.Y. acquired and analyzed the data and drafted the manuscript; R.D. and Q.X.
659 performed data processing and investigation; Q.H., Y.L., and C.W. provided theoretical support; J.X. and Y.S.

660 discussed the results and revised the manuscript; Y.L. acquired funding; all co-authors reviewed and approved the
 661 final version of the manuscript.

662

663 **Competing interests**

664 The authors declare that they have no conflict of interest.

665

666 **References**

- 667 Ansmann, A., Muellera, D., Wandinger, U., & Mamouri, R.E. (2013). Lidar profiling of aerosol optical and microphysical
 668 properties from space: Overview, review, and outlook. In, *1st International Conference on Remote Sensing and*
 669 *Geoinformation of the Environment (RSCy)*. Paphos, CYPRUS
- 670 Biuki, Z.A., Parvin, P., & Aghaei, M. (2022). Satellite remote sensing of particulate matter in the atmosphere of megacities:
 671 A case study of Tehran, Iran. *Atmospheric Pollution Research*, *13*, <http://doi.org/10.1016/j.apr.2022.101545>.
- 672 Cairo, F., Di Liberto, L., Dionisi, D., & Snels, M. (2024). Understanding aerosol-cloud interactions through lidar techniques:
 673 A review. *Remote Sensing*, *16*, <http://doi.org/10.3390/rs16152788>.
- 674 Chen, C., Song, X., Wang, Z., Chen, Y., Wang, X., Bu, Z., Zhang, X., Zhuang, Q., Pan, X., Li, H., Zhang, F., Wang, X., Li,
 675 X., & Zheng, R. (2022). Calibration methods of atmospheric aerosol lidar and a case study of haze process. *Frontiers*
 676 *in Physics*, *10*, <http://doi.org/10.3389/fphy.2022.942926>.
- 677 Chen, W., Tang, H.Z., Zhao, H.M., & Yan, L. (2016). Analysis of aerosol properties in Beijing based on ground-based sun
 678 photometer and air quality monitoring observations from 2005 to 2014. *Remote Sensing*, *8*,
 679 <http://doi.org/10.3390/rs8020110>.
- 680 Chen, X., Yang, T., Wang, H.B., Wang, F.T., & Wang, Z.F. (2023). Variations and drivers of aerosol vertical characterization
 681 after clean air policy in China based on 7-years consecutive observations. *Journal of Environmental Sciences*, *125*,
 682 499-512, <http://doi.org/10.1016/j.jes.2022.02.036>.
- 683 Chen, Y., Bu, Z., Wang, X., Dai, Y., Li, Z., Lu, T., Liu, Y., & Wang, X. (2024a). Development and calibration of 532 nm
 684 standard aerosol lidar with low blind area. *Remote Sensing*, *16*, <http://doi.org/10.3390/rs16030570>.
- 685 Chen, Z., Ji, C., Mao, J., Wang, Z., Jiao, Z., Gao, L., Xiang, Y., & Zhang, T. (2024b). Downdraft influences on the
 686 differences of PM_{2.5} concentration: Insights from a mega haze evolution in the winter of northern China.
 687 *Environmental Research Letters*, *19*, <http://doi.org/10.1088/1748-9326/ad1229>.
- 688 Chouza, F., Reitebuch, O., Gross, S., Rahm, S., Freudenthaler, V., Toledano, C., & Weinzierl, B. (2015). Retrieval of aerosol
 689 backscatter and extinction from airborne coherent Doppler wind lidar measurements. *Atmospheric Measurement*

- 690 *Techniques*, 8, 2909-2926, <http://doi.org/10.5194/amt-8-2909-2015>.
- 691 Dai, F., Chen, M., & Yang, B. (2020). Spatiotemporal variations of PM_{2.5} concentration at the neighborhood level in five
692 Chinese megacities. *Atmospheric Pollution Research*, 11, 190-202, <http://doi.org/10.1016/j.apr.2020.03.010>.
- 693 Deng, X.L., Chen, J., Dai, R., Zhai, Z.F., He, D.Y., Zhao, L., Jin, X.L., & Zhang, J.P. (2023). The effects of planetary
694 boundary layer features on air pollution based on ERA5 data in East China. *Atmosphere*, 14,
695 <http://doi.org/10.3390/atmos14081273>.
- 696 Fan, G., Zhang, B., Zhang, T., Fu, Y., Pei, C., Lou, S., Li, X., Chen, Z., & Liu, W. (2024). Accuracy evaluation of differential
697 absorption lidar for ozone detection and intercomparisons with other instruments. *Remote Sensing*, 16,
698 <http://doi.org/10.3390/rs16132369>.
- 699 Fan, S., Gao, C.Y., Wang, L., Yang, Y., Liu, Z., Hu, B., Wang, Y., Wang, J., & Gao, Z. (2021). Elucidating roles of near-
700 surface vertical layer structure in different stages of PM_{2.5} pollution episodes over urban Beijing during 2004-2016.
701 *Atmospheric Environment*, 246, <http://doi.org/10.1016/j.atmosenv.2020.118157>.
- 702 Fang, Z., Yang, H., Li, C., Kuang, Z., Xu, X., & Jin, H. (2024). Reveal persistent haze pollution episodes in Hefei: A
703 perspective from ground-based and satellite observation. *Air Quality Atmosphere and Health*, 17, 2555-2568,
704 <http://doi.org/10.1007/s11869-024-01587-2>.
- 705 Gao, F., Bergant, K., Filipcic, A., Forte, B., Hua, D.X., Song, X.Q., Stanic, S., Veberic, D., & Zavrtnik, M. (2011).
706 Observations of the atmospheric boundary layer across the land-sea transition zone using a scanning Mie lidar.
707 *Journal of Quantitative Spectroscopy & Radiative Transfer*, 112, 182-188, <http://doi.org/10.1016/j.jqsrt.2010.04.001>.
- 708 Gao, Y.-Q., Chen, Y., Liu, G.-D., & Zhang, J.-M. (2020). Investigating the influence of meteorological factors on particulate
709 matters: A case study based on path analysis. *Energy & Environment*, 31, 479-491,
710 <http://doi.org/10.1177/0958305x19876696>.
- 711 Garratt, J.R. (1994). Review: The atmospheric boundary layer. *Earth-Science Reviews*, 37, 89-134,
712 [http://doi.org/10.1016/0012-8252\(94\)90026-4](http://doi.org/10.1016/0012-8252(94)90026-4).
- 713 Gebauer, H., Floutsi, A.A., Haarig, M., Radenz, M., Engelmann, R., Althausen, D., Skupin, A., Ansmann, A., Zenk, C., &
714 Baars, H. (2024). Tropospheric sulfate from Cumbre Vieja (La Palma) observed over Cabo Verde contrasted with
715 background conditions: A lidar case study of aerosol extinction, backscatter, depolarization and lidar ratio profiles
716 at 355, 532 and 1064 nm. *Atmospheric Chemistry and Physics*, 24, 5047-5067, [http://doi.org/10.5194/acp-24-5047-](http://doi.org/10.5194/acp-24-5047-2024)
717 [2024](http://doi.org/10.5194/acp-24-5047-2024).
- 718 Haarig, M., Ansmann, A., Gasteiger, J., Kandler, K., Althausen, D., Baars, H., Radenz, M., & Farrell, D.A. (2017). Dry
719 versus wet marine particle optical properties: RH dependence of depolarization ratio, backscatter, and extinction

- 720 from multiwavelength lidar measurements during SALTRACE. *Atmospheric Chemistry and Physics*, 17, 14199-
721 14217, <http://doi.org/10.5194/acp-17-14199-2017>.
- 722 Han, X., & Cao, T. (2022). Urbanization level, industrial structure adjustment and spatial effect of urban haze pollution:
723 Evidence from China's Yangtze River Delta urban agglomeration. *Atmospheric Pollution Research*, 13,
724 <http://doi.org/10.1016/j.apr.2022.101427>.
- 725 He, G., Deng, T., Wu, D., Wu, C., Huang, X., Li, Z., Yin, C., Zou, Y., Song, L., Ouyang, S., Tao, L., & Zhang, X. (2021).
726 Characteristics of boundary layer ozone and its effect on surface ozone concentration in Shenzhen, China: A case
727 study. *Science of the Total Environment*, 791, <https://doi.org/10.1016/j.scitotenv.2021.148044>.
- 728 He, Y., Li, L., Wang, H., Xu, X., Li, Y., & Fan, S. (2022). A cold front induced co-occurrence of O₃ and PM_{2.5} pollution in
729 a Pearl River Delta city: Temporal variation, vertical structure, and mechanism. *Environmental Pollution*, 306,
730 <http://doi.org/10.1016/j.envpol.2022.119464>.
- 731 Huang, L., Chen, M.D., & Hu, J.L. (2016). Twelve-year trends of PM₁₀ and visibility in the Hefei metropolitan area of
732 China. *Advances in Meteorology*, 2016, <http://doi.org/10.1155/2016/4810796>.
- 733 Jin, X., Cai, X., Yu, M., Wang, X., Song, Y., Kang, L., Zhang, H., & Zhu, T. (2021). Mesoscale structure of the atmospheric
734 boundary layer and its impact on regional air pollution: A case study. *Atmospheric Environment*, 258,
735 <http://doi.org/10.1016/j.atmosenv.2021.118511>.
- 736 Kumar, V.R., Collins, R.L., & Yellapragada, B.K. (2024). Polarization lidar observations of diurnal and seasonal variations
737 in the atmospheric mixing layer above a tropical rural place gadanki, India. *Journal of Atmospheric and Solar-
738 Terrestrial Physics*, 263, <http://doi.org/10.1016/j.jastp.2024.106335>.
- 739 Li, H.D., Sodoudi, S., Liu, J.F., & Tao, W. (2020). Temporal variation of urban aerosol pollution island and its relationship
740 with urban heat island. *Atmospheric Research*, 241, <http://doi.org/10.1016/j.atmosres.2020.104957>.
- 741 Li, Q.H., Zhang, H.S., Jin, X.P., Cai, X.H., & Song, Y. (2022). Mechanism of haze pollution in summer and its difference
742 with winter in the North China Plain. *Science of the Total Environment*, 806,
743 <http://doi.org/10.1016/j.scitotenv.2021.150625>.
- 744 Li, X., Wang, Y., Shen, L., Zhang, H., Zhao, H., Zhang, Y., & Ma, Y. (2018). Characteristics of boundary layer structure
745 during a persistent haze event in the central Liaoning city Cluster, Northeast China. *Journal of Meteorological
746 Research*, 32, 302-312, <http://doi.org/10.1007/s13351-018-7053-6>.
- 747 Li, Y., Chen, Q.L., Zhao, H.J., Wang, L., & Tao, R. (2015). Variations in PM₁₀, PM_{2.5} and PM_{1.0} in an urban area of the
748 Sichuan basin and their relation to meteorological factors. *Atmosphere*, 6, 150-163,
749 <http://doi.org/10.3390/atmos6010150>.

- 750 Li, Y., Huang, T., Lee, H.F., Heo, Y., Ho, K.-F., & Yim, S.H.L. (2024). Integrating Doppler lidar and machine learning into
751 land-use regression model for assessing contribution of vertical atmospheric processes to urban PM_{2.5} pollution.
752 *Science of the Total Environment*, 952, <http://doi.org/10.1016/j.scitotenv.2024.175632>.
- 753 Liu, C., Huang, J., Wang, Y., Tao, X., Hu, C., Deng, L., Xu, J., Xiao, H.-W., Luo, L., Xiao, H.-Y., & Xiao, W. (2020).
754 Vertical distribution of PM_{2.5} and interactions with the atmospheric boundary layer during the development stage of
755 a heavy haze pollution event. *Science of the Total Environment*, 704, <http://doi.org/10.1016/j.scitotenv.2019.135329>.
- 756 Liu, J.L., Cai, P.L., Dong, J., Wang, J.S., Li, R.K., & Song, X.F. (2021). Assessment of the dynamic exposure to PM_{2.5}
757 based on hourly cell phone location and land use regression model in Beijing. *International Journal of*
758 *Environmental Research and Public Health*, 18, <http://doi.org/10.3390/ijerph18115884>.
- 759 Liu, T.T., Gong, S.L., He, J.J., Yu, M., Wang, Q.F., Li, H.R., Liu, W., Zhang, J., Li, L., Wang, X.G., Li, S.L., Lu, Y.L., Du,
760 H.T., Wang, Y.Q., Zhou, C.H., Liu, H.L., & Zhao, Q.C. (2017). Attributions of meteorological and emission factors
761 to the 2015 winter severe haze pollution episodes in China's Jing-Jin-Ji area. *Atmospheric Chemistry and Physics*,
762 17, 2971-2980, <http://doi.org/10.5194/acp-17-2971-2017>.
- 763 Liu, Z., Xiang, Y., Pan, Y., Zhang, T., Xu, W., & Li, L. (2024). Unveiling 3-D evolution and mechanisms of ozone pollution
764 in Changzhou, China: Insights from lidar observations and modelling. *Environmental Pollution*, 359, 124556,
765 <http://doi.org/10.1016/j.envpol.2024.124556>.
- 766 Liu, Z.R., Hu, B., Wang, L.L., Wu, F.K., Gao, W.K., & Wang, Y.S. (2015). Seasonal and diurnal variation in particulate
767 matter (PM₁₀ and PM_{2.5}) at an urban site of Beijing: analyses from a 9-year study. *Environmental Science and*
768 *Pollution Research*, 22, 627-642, <http://doi.org/10.1007/s11356-014-3347-0>.
- 769 Ma, P., Zhang, Z., Zhang, Y., Lamu, Y., & Za, D. (2023). Effect of meteorological conditions on PM₁₀ concentrations in
770 the middle reaches of the Yarlung Zangbo River, Tibet Plateau. *Theoretical and Applied Climatology*, 151, 725-737,
771 <http://doi.org/10.1007/s00704-022-04330-y>.
- 772 Mehta, M., Khushboo, R., Raj, R., & Singh, N. (2021). Spaceborne observations of aerosol vertical distribution over Indian
773 mainland (2009-2018). *Atmospheric Environment*, 244, <http://doi.org/10.1016/j.atmosenv.2020.117902>.
- 774 Miao, Y.C., Guo, J.P., Liu, S.H., Zhao, C., Li, X.L., Zhang, G., Wei, W., & Ma, Y.J. (2018). Impacts of synoptic condition
775 and planetary boundary layer structure on the trans-boundary aerosol transport from Beijing-Tianjin-Hebei region
776 to northeast China. *Atmospheric Environment*, 181, 1-11, <http://doi.org/10.1016/j.atmosenv.2018.03.005>.
- 777 Mishra, A.K., & Shibata, T. (2012). Climatological aspects of seasonal variation of aerosol vertical distribution over central
778 Indo-Gangetic belt (IGB) inferred by the space-borne lidar CALIOP. *Atmospheric Environment*, 46, 365-375,
779 <http://doi.org/10.1016/j.atmosenv.2011.09.052>.

- 780 Ou, J., Hu, Q., Liu, H., Hong, Q., Xing, C., Tan, W., Lin, H., Wang, X., Xu, H., Zhu, P., & Liu, W. (2021). Vertical
781 characterization and potential sources of aerosols in different seasons over the Yangtze River Delta using ground-
782 based MAX-DOAS. *Environmental Pollution*, 279, <http://doi.org/10.1016/j.envpol.2021.116898>.
- 783 Qian, Z., Li, L., Lin, X., Sun, R., & Chen, Y. (2024). Spatial and temporal variation of PM_{2.5} and the influence of vegetation
784 in the Yangtze River Delta region. *Atmospheric Pollution Research*, 15, <http://doi.org/10.1016/j.apr.2024.102266>.
- 785 Shen, L., Cheng, Y., Bai, X., Dai, H., Wei, X., Sun, L., Yang, Y., Zhang, J., Feng, Y., Li, Y.J., Chen, D.-R., Liu, J., & Gui,
786 H. (2022). Vertical profile of aerosol number size distribution during a haze pollution episode in Hefei, China.
787 *Science of the Total Environment*, 814, <http://doi.org/10.1016/j.scitotenv.2021.152693>.
- 788 Shi, C.N., Yuan, R.M., Wu, B.W., Meng, Y.J., Zhang, H., Zhang, H.Q., & Gong, Z.Q. (2018). Meteorological conditions
789 conducive to PM_{2.5} pollution in winter 2016/2017 in the Western Yangtze River Delta, China. *Science of the Total*
790 *Environment*, 642, 1221-1232, <http://doi.org/10.1016/j.scitotenv.2018.06.137>.
- 791 Shim, K., Kim, M.-H., Lee, H.-J., Nishizawa, T., Shimizu, A., Kobayashi, H., Kim, C.-H., & Kim, S.-W. (2022).
792 Exacerbation of PM_{2.5} concentration due to unpredictable weak Asian dust storm: A case study of an extraordinarily
793 long-lasting spring haze episode in Seoul, Korea. *Atmospheric Environment*, 287,
794 <http://doi.org/10.1016/j.atmosenv.2022.119261>.
- 795 Sun, W.B., Liu, Z.Y., Videen, G., Fu, Q., Muinonen, K., Winker, D.M., Lukashin, C., Jin, Z.H., Lin, B., & Huang, J.P.
796 (2013). For the depolarization of linearly polarized light by smoke particles. *Journal of Quantitative Spectroscopy*
797 *& Radiative Transfer*, 122, 233-237, <http://doi.org/10.1016/j.jqsrt.2012.03.031>.
- 798 Sun, X., Zhao, T., Hu, J., Bai, Y., Meng, L., Yang, Q., Zhou, Y., & Fu, W. (2024a). Inverse effects of aerosol radiative
799 forcing on heavy PM_{2.5} pollution of local accumulation and regional transport over central China. *Science of the*
800 *Total Environment*, 917, <http://doi.org/10.1016/j.scitotenv.2024.170319>.
- 801 Sun, X., Zhou, Y., Zhao, T., Fu, W., Wang, Z., Shi, C., Zhang, H., Zhang, Y., Yang, Q., & Shu, Z. (2024b). Vertical
802 distribution of aerosols and association with atmospheric boundary layer structures during regional aerosol transport
803 over central China. *Environmental Pollution*, 362, <http://doi.org/10.1016/j.envpol.2024.124967>.
- 804 Tombrou, M., Dandou, A., Helmis, C., Akylas, E., Angelopoulos, G., Flocas, H., Assimakopoulos, V., & Soulakellis, N.
805 (2007). Model evaluation of the atmospheric boundary layer and mixed-layer evolution. *Boundary-Layer*
806 *Meteorology*, 124, 61-79, <http://doi.org/10.1007/s10546-006-9146-5>.
- 807 Vakkari, V., Baars, H., Bohlmann, S., Bühl, J., Komppula, M., Mamouri, R.-E., & O'Connor, E.J. (2021). Aerosol particle
808 depolarization ratio at 1565 nm measured with a Halo Doppler lidar. *Atmospheric Chemistry and Physics*, 21, 5807-
809 5820, <http://doi.org/10.5194/acp-21-5807-2021>.

- 810 Wang, H., Sun, Z., Li, H., Gao, Y., Wu, J., & Cheng, T. (2018). Vertical-distribution characteristics of atmospheric aerosols
811 under different thermodynamic conditions in Beijing. *Aerosol and Air Quality Research*, *18*, 2775-2787,
812 <http://doi.org/10.4209/aaqr.2018.03.0078>.
- 813 Wang, J., Wang, H., Zhang, C., Wang, Y., Zhang, Y., Zhou, J., Xu, W., Whalley, L.K., Dyson, J.E., Slater, E.J., Xing, C.,
814 Chi, S., Wang, Y., Wang, L., Yu, X., Zeng, L., Lin, W., Zhao, W., Heard, D.E., Song, S., & Ye, C. (2025). Ozone
815 production underestimation over the Tibetan Plateau: The role of NO_x and OVOCs modeling uncertainties. *Journal*
816 *of Geophysical Research-Atmospheres*, *130*, <http://doi.org/10.1029/2025jd043321>.
- 817 Wang, J.L., Zhang, Y.H., Shao, M., Liu, X.L., Zeng, L.M., Cheng, C.L., & Xu, X.F. (2004). Chemical composition and
818 quantitative relationship, between meteorological condition and fine particles in Beijing. *Journal of Environmental*
819 *Sciences*, *16*, 860-864
- 820 Wang, L.Y., Lyu, B.L., & Bai, Y.Q. (2020a). Aerosol vertical profile variations with seasons, air mass movements and local
821 PM_{2.5} levels in three large China cities. *Atmospheric Environment*, *224*,
822 <http://doi.org/10.1016/j.atmosenv.2020.117329>.
- 823 Wang, M., & Wang, H. (2021). Spatial distribution patterns and influencing factors of PM_{2.5} pollution in the Yangtze River
824 Delta: Empirical analysis based on a GWR model. *Asia-Pacific Journal of Atmospheric Sciences*, *57*, 63-75,
825 <http://doi.org/10.1007/s13143-019-00153-6>.
- 826 Wang, M., Wei, T., Lolli, S., Wu, K., Wang, Y., Hu, H., Yuan, J., Tang, D., & Xia, H. (2024). A long-term Doppler wind
827 lidar study of heavy pollution episodes in western Yangtze River Delta region, China. *Atmospheric Research*, *310*,
828 <http://doi.org/10.1016/j.atmosres.2024.107616>.
- 829 Wang, Z., Liu, C., Hu, Q.H., Dong, Y.S., Liu, H.R., Xing, C.Z., & Tan, W. (2021). Quantify the Contribution of Dust and
830 Anthropogenic Sources to Aerosols in North China by Lidar and Validated with CALIPSO. *Remote Sensing*, *13*,
831 <http://doi.org/10.3390/rs13091811>.
- 832 Wang, Z., Liu, C., Xie, Z.Q., Hu, Q.H., Andreae, M.O., Dong, Y.S., Zhao, C., Liu, T., Zhu, Y.Z., Liu, H.R., Xing, C.Z., Tan,
833 W., Ji, X.G., Lin, J.N., & Liu, J.G. (2020b). Elevated dust layers inhibit dissipation of heavy anthropogenic surface
834 air pollution. *Atmospheric Chemistry and Physics*, *20*, 14917-14932, <http://doi.org/10.5194/acp-20-14917-2020>.
- 835 Xiang, Y., Zhang, T., Liu, J., Wan, X., Loewen, M., Chen, X., Kang, S., Fu, Y., Lv, L., Liu, W., & Cong, Z. (2021). Vertical
836 profile of aerosols in the Himalayas revealed by lidar: New insights into their seasonal/diurnal patterns, sources,
837 and transport*. *Environmental Pollution*, *285*, <http://doi.org/10.1016/j.envpol.2021.117686>.
- 838 Xiong, K., Xie, X., Mao, J., Wang, K., Huang, L., Li, J., & Hu, J. (2023). Improving the accuracy of O₃ prediction from a
839 chemical transport model with a random forest model in the River Delta China. *Environmental Pollution*, *319*,

- 840 <http://doi.org/10.1016/j.envpol.2022.120926>.
- 841 Yang, S.M., Ma, Y.J., Zhang, W.Y., Lin, Z., Lu, Z.G., Zhou, X.J., Ren, Y.Z., Ren, X.B., Peng, K.C., Tan, Y.L., Wei, Y.M.,
842 Ahmad, M., Zhao, D.D., Kong, L.B., Ma, Y.N., Tian, Y.L., & Xin, J.Y. (2025). The interaction of atmospheric
843 boundary layer and PM pollution in Mongolian Plateau: Implication for the threshold control strategy. *Atmospheric*
844 *Research*, 316, <http://doi.org/10.1016/j.atmosres.2025.107937>.
- 845 Yang, Y.J., Yim, S.H.L., Haywood, J., Osborne, M., Chan, J.C.S., Zeng, Z.L., & Cheng, J.C.H. (2019). Characteristics of
846 heavy particulate matter pollution events over Hong Kong and their relationships with vertical wind profiles using
847 high-time-resolution Doppler lidar measurements. *Journal of Geophysical Research-Atmospheres*, 124, 9609-9623,
848 <http://doi.org/10.1029/2019jd031140>.
- 849 Yang, Z., Wang, Y., Xu, X.-H., Yang, J., & Ou, C.-Q. (2022). Quantifying and characterizing the impacts of PM_{2.5} and
850 humidity on atmospheric visibility in 182 Chinese cities: A nationwide time-series study. *Journal of Cleaner*
851 *Production*, 368, <http://doi.org/10.1016/j.jclepro.2022.133182>.
- 852 Yu, H.J., Wang, Y.J., Peng, Q., Shao, Y.Q., Duan, C.M., Zhu, Y.F., Dong, S.R., Li, C.L., Shi, Y., Zhang, N., Zheng, Y.Y.,
853 Chen, Y., Jiang, Q.W., Zhong, P.S., & Zhou, Y.B. (2020). Influence of coarse particulate matter on chickenpox in
854 Jiading District, Shanghai, 2009-2018: A distributed lag non-linear time series analysis. *Environmental Research*,
855 190, <http://doi.org/10.1016/j.envres.2020.110039>.
- 856 Yu, S., Liu, D., Xu, J., Wang, Z., Wu, D., Shan, Y., Shao, J., Mao, M., Qian, L., Wang, B., Xie, C., & Wang, Y. (2021).
857 Optical properties and seasonal distribution of aerosol layers observed by lidar over Jinhua, southeast China.
858 *Atmospheric Environment*, 257, <http://doi.org/10.1016/j.atmosenv.2021.118456>.
- 859 Zhan, Y., Xie, M., Zhuang, B., Gao, D., Zhu, K., Lu, H., Wang, T., Li, S., Li, M., Luo, Y., & Zhao, R. (2024). Particle-
860 ozone complex pollution under diverse synoptic weather patterns in the Yangtze River Delta region: Synergistic
861 relationships and the effects of meteorology and chemical compositions. *Science of the Total Environment*, 946,
862 174365, <http://doi.org/10.1016/j.scitotenv.2024.174365>.
- 863 Zhang, T., Che, H.Z., Gong, Z.Q., Wang, Y.Q., Wang, J.Z., Yang, Y.Q., Gui, K., & Guo, B. (2020a). The two-way feedback
864 effect between aerosol pollution and planetary boundary layer structure on the explosive rise of PM_{2.5} after the "Ten
865 Statements of Atmosphere" in Beijing. *Science of the Total Environment*, 709,
866 <http://doi.org/10.1016/j.scitotenv.2019.136259>.
- 867 Zhang, Y., Guo, J., Yang, Y., Wang, Y., & Yim, S.H.L. (2020b). Vertical wind shear modulates particulate matter pollutions:
868 A perspective from radar wind profiler observations in Beijing, China. *Remote Sensing*, 12,
869 <http://doi.org/10.3390/rs12030546>.

870 Zhong, J., Zhang, X., Dong, Y., Wang, Y., Liu, C., Wang, J., Zhang, Y., & Che, H. (2018). Feedback effects of boundary-
871 layer meteorological factors on cumulative explosive growth of PM_{2.5} during winter heavy pollution episodes in
872 Beijing from 2013 to 2016. *Atmospheric Chemistry and Physics*, 18, 247-258, [http://doi.org/10.5194/acp-18-247-](http://doi.org/10.5194/acp-18-247-2018)
873 [2018](http://doi.org/10.5194/acp-18-247-2018).
874